A fully coupled dynamic water-mooring line system: Numerical implementation and applications

Xiangcou Zheng [*], Mohammed Seaid, Ashraf S. Osman

Department of Engineering, University of Durham, South Road, DH1 3LE, United Kingdom

ARTICLE INFO

ABSTRACT

Several numerical challenges exist in the analysis of water-mooring line systems which require robust, yet practical, methods to address this type of fully coupled nonlinear dynamic problems. The present study proposes a novel class of numerical techniques for the formulation and implementation of a fully coupled dynamic system which involves water flows and catenary mooring line system. In particular, the three-dimensional water flow model is replaced by a simplified multilayer shallow water system with mass exchange terms between the layers including frictional forces at the bed topography and wind-driven forces at the water free-surface. Coupling conditions between the multilayer shallow water model and the mooring line system are also investigated in the current work. As numerical solvers we implement a fast finite volume method for the multilayer shallow water equations and a nonlinear dynamic analysis for the mooring line based on elastic catenary cable elements. Efficient calculations of the interaction forces between the shallow water flow and the submerged mooring line system and associated numerical implementations are also discussed. The accuracy and computational advantages of the proposed fully coupled system are verified using a series of well-established benchmark problems and wind-driven flows over both flat and non-flat beds. The computational results obtained show high performance the developed model and demonstrate the ability of the method to simulate fully coupled dynamic water-mooring line systems.

1. Introduction

Most offshore wind turbine platforms with fixed foundations are frequently installed in coastal areas. However, wind features (such as wind speed, direction and turbulence) tend to be considerably improved in the open-sea areas where water depth usually becomes deeper. Floating Offshore Wind Turbine (FOWT) platforms with mooring systems are more cost-effective and have significant advantages over those mounted on fixed offshore wind turbine platforms, see for example Maffra et al. (2003). For FOWT platforms in deep-sea areas, traditional steel wire ropes and chain mooring lines are required to be replaced by synthetic fibre ropes with lesser weights (API, 2001). Needless to mention that the synthetic fibre ropes exhibit significant geometric non-linearity, which yields significant influence on their mechanical behaviour, see Li and Choung (2021b) and Li et al. (2016) among others. A wide literature on mooring models has been published using an assumption of linear stiffness, see for instance (Harnois et al., 2015; Li and Choung, 2017; Li et al., 2018; Soulard et al., 2013; Yang et al., 2014) whereas, a relatively limited number of studies have focused on the mooring models with a nonlinear stiffness, see for example Thai and Kim (2011) and Abad et al. (2013). Bhinder et al. (2015) adopted commercial

softwares to examine the influence of nonlinear stiffness on the coupled platform responses. The well-established lumped mass method has been used in Xiong et al. (2018) to achieve the viscoelasticity and nonlinear stiffness of a synthetic fibre rope in the taut-leg mooring systems. Thai and Kim (2011) proposed a spatial two-node catenary cable element for the nonlinear analysis of cable structures based on the exact analytical expressions of elastic catenary. Note that the proposed cable system requires fewer degrees of freedom and it exactly considers the nonlinear effects of the cable, which is also preferred in this study for modelling the dynamic motion of mooring lines.

Modelling water flows in stratified geophysical domains as those considered in this study, is mainly based on the formulation and solution of appropriate equations of continuity and dynamics of water. In practice, free-surface flows involve three-dimensional turbulent Newtonian fluids in complex geometrical domains with moving boundaries. For instance, the incompressible Navier–Stokes equations have been widely considered as highly accurate systems for modelling and simulating water flows, see for example Codina (1999) and Yan et al. (2017). However, for most free-surface flows, these partial differential equations are difficult to solve mainly because the pressure in

---

* Corresponding author.
  E-mail addresses: xczheng@csu.edu.cn (X. Zheng), m.seaid@durham.ac.uk (M. Seaid), ashraf.osman@durham.ac.uk (A.S. Osman).

these equations is hydrostatic and the domain boundaries are moving within the free-surface flow. Assuming a hydrostatic pressure and the vertical scale is smaller than other scales in the flow domain, the three-dimensional Navier–Stokes equations can be replaced by a depth-averaged system well known in the literature by shallow water equations, see for example Abbott (1979). In fact, shallow water equations have been widely used for modelling many free-surface flows in hydraulics such as open channel flows, floods in rivers and tidal flows in coastal regions among others, see Ozgen et al. (2016) among others. However, these depth-averaged equations fail to resolve the vertical velocity as the bed friction is derived in terms of the mean flow velocity only instead of the near-bed velocity. Therefore, the three-dimensional equations are required for an accurate representation of free-surface flows, especially for wind-driven recirculation flows and for solution of near-field problems involving mooring-line systems. In recent years, research in free-surface flows has been shifted to overcome drawbacks of the depth-averaged equations related to the use of single velocity profiles for the entire depth in the flow domain. Hence, the introduction of multilayer shallow water models as an alternative for the conventional single-layer shallow water equations for modelling geophysical free-surface flows, see for example Audusse et al. (2011a,b) and Bonaventura et al. (2018). In this class of multilayer models, the P_0 finite element method is used to discretize the vertical velocity in the three-dimensional incompressible Navier–Stokes equations. It has also been shown in Audusse et al. (2011a, 2014) and Izem and Seaid (2021) that these multilayer shallow water models drastically reduce the computational costs required to solve the full three-dimensional incompressible Navier–Stokes equations subject to free-surface boundary conditions but still capturing the stratified flow velocities since the pressure distribution remains hydrostatic. In the present work, to model the free-surface flow in water-mooring line systems, we consider a layered flow domain made of multiple shallow water systems with different water heights but fully coupled through mass-exchange terms between the embedded layers. The proposed model also includes frictional forces at the bed topography and wind shear stresses at the water free-surface generating vertical velocity distribution which contributes to the dynamics of mooring-line systems considered in this study. Interactions between the flow field and mooring-line system are also investigated in the current work and transfer coupling conditions between the two dynamics are also developed.

The main objective of the present study is to propose a novel fully coupled model for solving water-mooring line systems in accurate and efficient manners. To achieve this objective, we propose the multilayer shallow water equations for free-surface flows coupled with the elastic catenary cable elements for nonlinear dynamics of the mooring lines. Frictional source terms are included in each layer of the water domain for modelling the interaction between the shallow water flow and the submerged mooring line system. The numerical solution of the coupled equations is not trivial and it presents difficulties due to their nonlinearity, coupling between the free-surface equations and the equations governing the mooring-line dynamics, and non-flat bed topography. Furthermore, difficulties in solving multilayer shallow water equations are also related to the presence of source terms involving derivatives of the unknown variables which makes the system non-conservative and eventually non-hyperbolic. Thus, numerical methods designed for solving the conventional single-layer shallow water equations would yield instabilities if they are applied to each layer separately in the multilayer shallow water system. In the current work, to solve the multilayer shallow water equations we adapt the finite volume characteristics (FVC) method introduced in Benkhaldoun and Seaid (2010). The FVC method provides a fast and accurate solver for the multilayer shallow water system as it does not require Riemann-problem solvers for the reconstruction of numerical fluxes, see in Audusse et al. (2014) and Benkhaldoun et al. (2014). A second-order splitting operator along with an explicit Runge–Kutta scheme is also presented in this study for the time integration of multilayer shallow water equations. The

numerical solution of nonlinear dynamics of the mooring line is carried out using a group of elastic catenary cable elements for space discretization and an implicit scheme using Newton's iterations for the time integration. A class of robust velocity/acceleration projections and interpolation procedures are proposed for the transfer of coupling terms between both models and full description of the coupled algorithm is also discussed in the present work. Several numerical examples are presented to verify the considered water-mooring line systems. First, we examine the performance of the proposed numerical techniques using well-established benchmark problems in free-surface flows and mooring lines. Then, we demonstrate the capability of the coupled model to accurately resolve lateral and vertical distributions of velocities for wind-driven recirculation flows over flat and non-flat beds in the presence of mooring lines.

This paper is organized as follows. Description of the dynamic motion for shallow water flows and mooring line systems is presented in Section 2. This section covers the governing equations for multilayer shallow water flows and nonlinear motion of the mooring line system. Section 3 is devoted to the numerical formulation and implementation of the fully coupled dynamic multilayer shallow water-mooring line system. We consider a fast and robust second-order finite volume method for the multilayer shallow water flows whereas, a fully dynamic nonlinear catenary cable element for the mooring line is implemented for the shallow water flows. Details on the dynamic coupling algorithm between the shallow water and mooring line are also discussed in this section. In Section 4, we present numerical results for several examples of coupled multilayer shallow water flows and nonlinear motion of the mooring line system. The proposed fully coupled system is shown to enjoy the expected accuracy as well as the efficiency. Concluding remarks are drawn in Section 5.

2. Governing equations for multilayer shallow water and mooring line system

In the current work, we are interested in water flows occurring on the free-surface where assumptions of shallow water flows are applied coupled to the mooring line dynamics. In this section we present mathematical equations governing dynamics of both systems and we introduce coupling equations for transfer conditions between their dynamics.

2.1. Multilayer shallow water equations for free-surface water flows

As illustrated in Fig. 1, the water body bounded by a non-flat bottom topography $Z(x)$ and a free water surface is vertically discretized into N fictitious layers. Following Audusse et al. (2011a,b), using a vertical P_0 discretization of the horizontal velocity u, the well-known three-dimensional hydrostatic incompressible Navier–Stokes equations with free-surface yield the so-called multilayer shallow water equations. In this section, only the derivations of these equations that directly related to a complete description of the fully coupled system are provided, and more details can be found in Audusse et al. (2011a,b). Thus, similar to the conventional single-layer shallow water problems, the governing equations for multilayer shallow water models with additional terms for exchanging momentum between the layers are written as

$$\frac{\partial H}{\partial t} + \sum_{\beta=1}^{N} \frac{\partial}{\partial x} \left(l_\beta H u_\beta \right) = 0,$$

(1)

$$\frac{\partial}{\partial t} \left(l_\beta H u_\beta \right) + \frac{\partial}{\partial x} \left(l_\beta H u_\beta^2 + \frac{1}{2} g l_\beta H^2 \right) = -g l_\beta H \frac{\partial Z}{\partial x} + S_\beta^u + S_\beta^\mu + S_\beta^b$$
$$+ S_\beta^w + S_\beta^m, \qquad \beta = 1, 2, \dots, N,$$

where the subscript β defines the βth water layer, $H(t, x)$ is the water height of the whole flow system, $u_\beta(t, x)$ is the local velocity of the βth layer, g is the gravitational acceleration, $Z(x)$ is the bed topography,

and l_β is the ratio between the water height $h_\beta(t,x)$ of βth layer and the total water height defined as

$$l_\beta > 0, \qquad \sum_{\beta=1}^{N} l_\beta = 1,$$

with the water height $h_\beta(t,x)$ of the βth layer is defined by

$$h_\beta = l_\beta H, \qquad \beta = 1, 2, \dots, N.$$

In Eq. (1), the source term S_β^u represents the momentum exchange between the water layers. Following the vertical P_0 discretization of horizontal velocity, S_β^u is defined as

$$S_\beta^u = u_{\beta+\frac{1}{2}} \mathcal{M}_{\beta+\frac{1}{2}} - u_{\beta-\frac{1}{2}} \mathcal{M}_{\beta-\frac{1}{2}}, \qquad (2)$$

where the mass exchange terms $\mathcal{M}_{\beta-\frac{1}{2}}$ and $\mathcal{M}_{\beta+\frac{1}{2}}$ are evaluated using

$$\mathcal{M}_{\beta-\frac{1}{2}} = \begin{cases} 0, & \beta = 1, \\ \sum_{i=1}^{\beta} \left(\dfrac{\partial (h_i u_i)}{\partial x} - l_i \sum_{j=1}^{N} \dfrac{\partial (h_j u_j)}{\partial x} \right), & \beta = 2, 3 \dots, N, \end{cases} \qquad (3)$$

and

$$\mathcal{M}_{\beta+\frac{1}{2}} = \begin{cases} \sum_{i=1}^{\beta} \left(\dfrac{\partial (h_i u_i)}{\partial x} - l_i \sum_{j=1}^{N} \dfrac{\partial (h_j u_j)}{\partial x} \right), & \beta = 1, 2, \dots, N-1, \\ 0, & \beta = N, \end{cases} \qquad (4)$$

respectively. Here, the interface velocities $u_{\beta-\frac{1}{2}}$ and $u_{\beta+\frac{1}{2}}$ are computed according to the sign of mass-exchange terms in Eqs. (3) and (4) as

$$u_{\beta-\frac{1}{2}} = \begin{cases} u_{\beta-1}, & \mathcal{M}_{\beta-\frac{1}{2}} \geq 0, \\ u_\beta, & \mathcal{M}_{\beta-\frac{1}{2}} < 0, \end{cases} \qquad u_{\beta+1/2} = \begin{cases} u_\beta, & \mathcal{M}_{\beta+\frac{1}{2}} \geq 0, \\ u_{\beta+1}, & \mathcal{M}_{\beta+\frac{1}{2}} < 0. \end{cases} \qquad (5)$$

The vertical kinematic eddy viscosity term S_β^μ in Eq. (1) represents the relative friction between neighbouring water layers and it is defined as

$$S_\beta^\mu = \begin{cases} 2\nu \dfrac{u_{\beta+1} - u_\beta}{(l_{\beta+1} + l_\beta) H}, & \beta = 1, \\ 2\nu \dfrac{u_{\beta+1} - u_\beta}{(l_{\beta+1} + l_\beta) H} - 2\nu \dfrac{u_\beta - u_{\beta-1}}{(l_\beta + l_{\beta-1}) H}, & \beta = 2, 3, \dots, N-1, \\ 2\nu \dfrac{u_\beta - u_{\beta-1}}{(l_\beta + l_{\beta-1}) H}, & \beta = N, \end{cases} \qquad (6)$$

where ν is the eddy viscosity. Similarly, the external friction terms S_β^b and S_β^w in Eq. (1) are defined by

$$S_\beta^b = \begin{cases} -g M_b^2 \dfrac{u_1 |u_1|}{H^{1/3}}, & \beta = 1, \\ 0, & \beta = 2, 3, \dots, N, \end{cases}$$

$$S_\beta^w = \begin{cases} 0, & \beta = 1, 2, \dots, N-1, \\ \sigma_s^2 \rho_a \dfrac{V_{\text{wind}} |V_{\text{wind}}|}{H}, & \beta = N, \end{cases} \qquad (7)$$

where M_b is the Manning's roughness coefficient at the bed, V_{wind} is the wind velocity at 10 m above the free water surface, σ_s is the wind stress coefficient, and ρ_a is the air density. Note that in Eq. (1), the bed-friction forcing term S_β^b is acting only on the lower layer whereas, the wind-driven forcing term S_β^w is only acting on the upper layer.

To account for effects of the mooring line on the shallow water flow in the proposed fully coupled system, the final source term S_β^m in the right-hand side of Eq. (1) refers to the frictional force acting on the shallow water owing to the presence of mooring line system. This term follows a similar mechanism as for the calculation of wind-driven forces
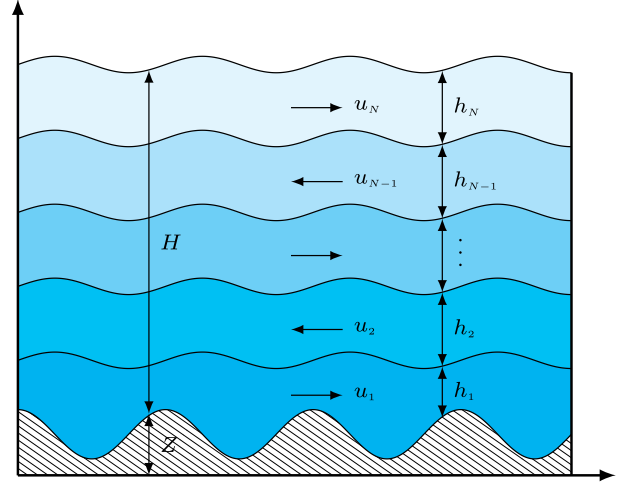

Fig. 1. Schematic illustration of the multilayer shallow water system.
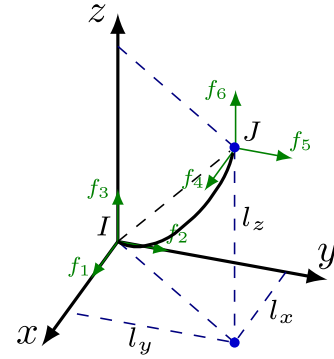

Fig. 2. An elastic catenary cable element supported by two end points I and J in the three space dimensions.

and it is defined as

$$S_\beta^m = \sigma_m^2 \rho_w \frac{V_{m,c} |V_{m,c}|}{\sum_{i=1}^{\beta} l_i H}, \qquad \beta = 1, 2, \dots, N, \qquad (8)$$

where σ_m is the Manning's roughness coefficient of the mooring line, $V_{m,c}$ is the velocity field mapping from the mooring line to the water system, and its determination is discussed in the section below. More details regarding the determination of the frictional force are elaborated in Section 3.

2.2. Governing equations for the mooring line system

This section is devoted to some fundamentals regarding the modelling of elastic catenary cable elements for the nonlinear simulation of the mooring line system. To achieve this purpose, the elastic catenary cable elements proposed in Thai and Kim (2011) are adopted in this study. For a compact description, only those details essential to a full understanding of the numerical implementation are given here and more descriptions and further links to the adopted catenary cable elements can be found in previous studies such as Abad et al. (2013) and Thai and Kim (2011) among others. As shown in Fig. 2, the suspended cable element (in three space dimensions) is assumed to be supported by two end points I and J, and their Cartesian coordinates are defined by $(0,0,0)^\top$ and $(l_x, l_y, l_z)^\top$, respectively. Three main uniform distributed loads w_i ($i = 1, 2$ and 3) are separately applied along three global directions, namely, x, y, and z directions. In what follows,

the cable elements are assumed to be perfectly elastic and flexible under their own self-weight along its length, and their cross-sectional areas remain constant during the whole computational process.

Let us assume that s and p are, respectively the Lagrangian coordinates of the undeformed and the deformed configurations of the cable element. Hence, the equilibrium equations for the cable element can be formulated as

$$T\left(\frac{dx}{dp}\right) = -\left(w_1 s + f_1\right),$$
$$T\left(\frac{dy}{dp}\right) = -\left(w_2 s + f_2\right), \tag{9}$$
$$T\left(\frac{dz}{dp}\right) = -\left(w_3 s + f_3\right),$$

where f_1, f_2, and f_3 are the projected components of the cable force at the starting node along the three global directions, and the cable tension T in the Lagrangian coordinates s of the undeformed configurations is given by

$$T(s) = \sqrt{\sum_{i=1}^{3} \left(w_i s + f_i\right)^2}. \tag{10}$$

For a perfect elastic cable element, the relationship between the cable tension T and the strain ε follows the well-known Hooke's law as

$$T = EA\left(\varepsilon - \varepsilon_T\right) = EA\left(\frac{dp - ds}{ds} - \alpha \Delta T\right), \tag{11}$$

where E is the elastic modulus, A the cross-sectional area of the cable, ε the total cable strain, ε_T the cable strain component related to the temperature change, α the linear thermal expansion coefficient, and ΔT the temperature change. Note that relationships between the Cartesian and Lagrangian coordinates under undeformed configuration are defined by

$$x(s) = \int_0^s dx = \int_0^s \frac{dx}{dp}\frac{dp}{ds}ds,$$
$$y(s) = \int_0^s dy = \int_0^s \frac{dy}{dp}\frac{dp}{ds}ds, \tag{12}$$
$$z(s) = \int_0^s dz = \int_0^s \frac{dz}{dp}\frac{dp}{ds}ds,$$

which are subjected to the following boundary conditions

$$x(0) = 0, \qquad y(0) = 0, \qquad z(0) = 0,$$
$$x(l_0) = l_x, \qquad y(l_0) = l_y, \qquad z(l_0) = l_z,$$

where l_0 is the initial unstrained length of the cable element. By substituting Eqs. (9)–(11) into Eq. (12), the following relationships are obtained

$$x(s) = \int_0^s \frac{-\left(w_1 s + f_1\right)}{\sqrt{\sum_{i=1}^{3}\left(w_i s + f_i\right)^2}}\left(\frac{\sqrt{\sum_{i=1}^{3}\left(w_i s + f_i\right)^2}}{EA} + (1 + \alpha \Delta T)\right)ds,$$

$$y(s) = \int_0^s \frac{-\left(w_2 s + f_2\right)}{\sqrt{\sum_{i=1}^{3}\left(w_i s + f_i\right)^2}}\left(\frac{\sqrt{\sum_{i=1}^{3}\left(w_i s + f_i\right)^2}}{EA} + (1 + \alpha \Delta T)\right)ds, \tag{13}$$

$$z(s) = \int_0^s \frac{-\left(w_3 s + f_3\right)}{\sqrt{\sum_{i=1}^{3}\left(w_i s + f_i\right)^2}}\left(\frac{\sqrt{\sum_{i=1}^{3}\left(w_i s + f_i\right)^2}}{EA} + (1 + \alpha \Delta T)\right)ds.$$

After applying the associated boundary conditions, the projection lengths l_x, l_y, and l_z can be formulated as functions of the internal

forces f_1, f_2, and f_3 using

$$l_x\left(f_1, f_2, f_3\right) = -\frac{l_0 f_1}{EA} - \frac{l_0^2 w_1}{2EA} + \frac{1 + \alpha \Delta T}{w^3}\left(ww_1\left(T_1 - T_2\right)\right.$$
$$\left. + \left(w^2 f_1 - \beta w_1\right)\left(\ln\left(\frac{\beta}{w} + T_1\right) - \ln\left(l_0 w + \frac{\beta}{w} + T_2\right)\right)\right),$$

$$l_y\left(f_1, f_2, f_3\right) = -\frac{l_0 f_2}{EA} - \frac{l_0^2 w_2}{2EA} + \frac{1 + \alpha \Delta T}{w^3}\left(ww_2\left(T_1 - T_2\right)\right.$$
$$\left. + \left(w^2 f_2 - \beta w_2\right)\left(\ln\left(\frac{\beta}{w} + T_1\right) - \ln\left(l_0 w + \frac{\beta}{w} + T_2\right)\right)\right), \tag{14}$$

$$l_z\left(f_1, f_2, f_3\right) = -\frac{l_0 f_3}{EA} - \frac{l_0^2 w_3}{2EA} + \frac{1 + \alpha \Delta T}{w^3}\left(ww_3\left(T_1 - T_2\right)\right.$$
$$\left. + \left(w^2 f_3 - \beta w_3\right)\left(\ln\left(\frac{\beta}{w} + T_1\right) - \ln\left(l_0 w + \frac{\beta}{w} + T_2\right)\right)\right),$$

where $w = \sqrt{\sum_{i=1}^{3} w_i^2}$, $\beta = \sum_{i=1}^{3} f_i w_i$, $T_1 = T(0)$, and $T_2 = T(l_0)$. It should be noted that the tangent stiffness matrix $\mathbf{K}$ and the internal force vector $\boldsymbol{F}_{int}$ of the catenary cable element can be determined by solving the system of Eq. (14). Therefore, differentiating both sides of Eq. (14), the differential projected components become

$$dl_x = \frac{\partial l_x}{\partial f_1}df_1 + \frac{\partial l_x}{\partial f_2}df_2 + \frac{\partial l_x}{\partial f_3}df_3,$$
$$dl_y = \frac{\partial l_y}{\partial f_1}df_1 + \frac{\partial l_y}{\partial f_2}df_2 + \frac{\partial l_y}{\partial f_3}df_3, \tag{15}$$
$$dl_x = \frac{\partial l_z}{\partial f_1}df_1 + \frac{\partial l_z}{\partial f_2}df_2 + \frac{\partial l_z}{\partial f_3}df_3,$$

and its compact matrix form is given by

$$\begin{bmatrix} dl_x \\ dl_y \\ dl_z \end{bmatrix} = \begin{bmatrix} \frac{\partial l_x}{\partial f_1} & \frac{\partial l_x}{\partial f_2} & \frac{\partial l_x}{\partial f_3} \\ \frac{\partial l_y}{\partial f_1} & \frac{\partial l_y}{\partial f_2} & \frac{\partial l_y}{\partial f_3} \\ \frac{\partial l_z}{\partial f_1} & \frac{\partial l_z}{\partial f_2} & \frac{\partial l_z}{\partial f_3} \end{bmatrix}\begin{bmatrix} df_1 \\ df_2 \\ df_3 \end{bmatrix} := [\mathbf{F}]\begin{bmatrix} df_1 \\ df_2 \\ df_3 \end{bmatrix}, \tag{16}$$

where $[\mathbf{F}]$ is known by the flexibility matrix of the considered element. More details regarding the calculation of the flexibility matrix can be found in Abad et al. (2013) and Thai and Kim (2011). Thus, after determining the flexibility matrix $[\mathbf{F}]$, the global tangent stiffness $[\mathbf{K}]$ in terms of six degrees of freedom is obtained by taking the inverse of the matrix $[\mathbf{F}]$ and it is assembled using the following form

$$[\mathbf{K}] = \begin{bmatrix} -[\mathbf{F}]^{-1} & [\mathbf{F}]^{-1} \\ [\mathbf{F}]^{-1} & -[\mathbf{F}]^{-1} \end{bmatrix}. \tag{17}$$

Once the internal force components f_1, f_2, and f_3 for the first end point are determined, the internal nodal forces f_4, f_5, and f_6 at the second end point are computed using

$$f_4 = -(w_1 l_0 + f_1),$$
$$f_5 = -(w_2 l_0 + f_2), \tag{18}$$
$$f_6 = -(w_3 l_0 + f_3).$$

In a similar manner, the internal force vector $\boldsymbol{F}^{int}$ for the catenary cable element is assembled as

$$\boldsymbol{F}^{int} = \begin{bmatrix} f_1 & f_2 & f_3 & f_4 & f_5 & f_6 \end{bmatrix}^\top. \tag{19}$$

Once the stiffness matrices and internal force vectors are determined, the length and sag of each cable segment are thus determined. More details regarding calculations of the cable lengths and sags can be found in Thai and Kim (2011). It should be mentioned that, when considering a fully coupled dynamic water-mooring line system, effects of shallow water flows on the dynamic motion of the mooring line system are required to be addressed, which is considered through
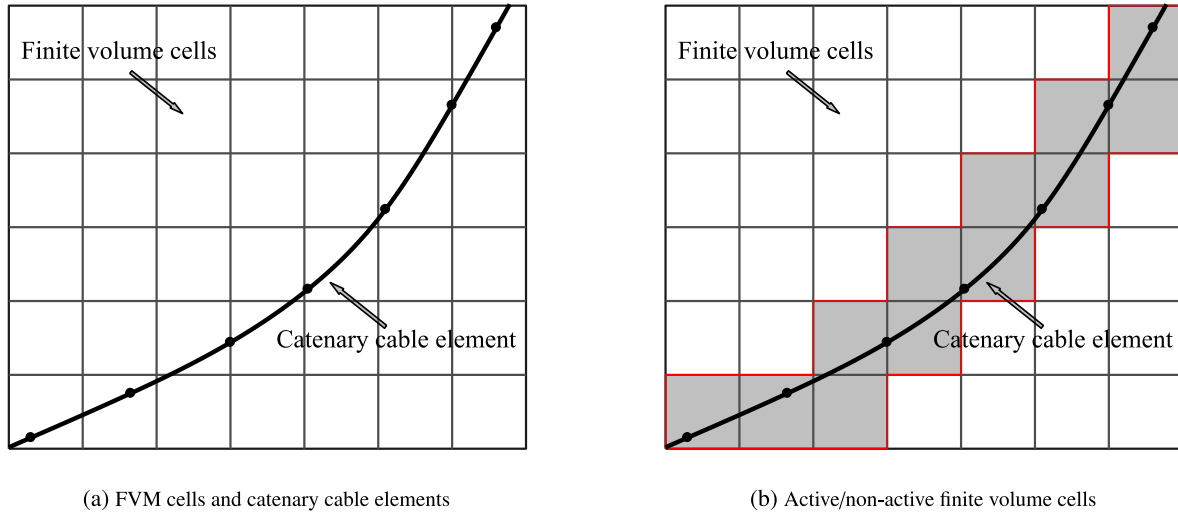
(a) FVM cells and catenary cable elements

(b) Active/non-active finite volume cells

Fig. 3. Spatial discretization of a multilayer shallow water and mooring line system.

a water current force term in the equation governing the dynamic motion of the mooring line. The calculation of the current force and its numerical implementation in the fully coupled system are discussed in Section 3.

3. Coupled dynamic multilayer shallow water-mooring line system

For a fully coupled multilayer shallow water-mooring line system, it is of great significance to address the interactions between the shallow water flow and the mooring line system. To achieve this goal, this section first introduces the computational procedure of contact/interaction forces in the fully coupled system, and then the numerical implementation of a coupled algorithm proposed in this study is formulated.

3.1. Numerical solution of the multilayer shallow water equations in the fully coupled system

When considering the fully coupled multilayer shallow water-mooring line system, the presence of a moving mooring line in the shallow water is expected to affect dynamics of the water flow. Here, in order to account for the influence of submerged mooring lines on the dynamic behaviour of the shallow water flow, a mooring line-friction force term S_β^m is introduced. In a similar manner as for the calculation of the wind-driven force, the mooring-line force term S_β^m considered in this study is defined by

$$S_\beta^m = \sigma_m^2 \rho_w \frac{V_\beta^{m,c} \left| V_\beta^{m,c} \right|}{H_\beta}, \tag{20}$$

where σ_m is the dimensionless drag coefficient of the mooring line, $V_\beta^{m,c}$ is the projected velocity of the mooring line at the βth layer in the water flow system, and H_β is the total height of the βth layer. Before calculating the source term S_β^m for each layer, it is required to determine the projected mooring line nodal velocities $V_\beta^{m,c}$.

As an illustration, Fig. 3 displays a typical schematic view of a structured spatial discretization of the multilayer shallow water equations and mooring line system, where the shallow water domain is discretized into a set of control volumes and the mooring line is discretized into a number of catenary cable elements (as shown in Fig. 3(a)). In order to account for the influence of dynamic motion in the mooring line on the dynamic behaviour of the shallow water flow, Fig. 3(b) identifies the active control volumes (*i.e.* cells that are intersected by the mooring line and shaded in dark grey colour). On the contrary,

those control volumes that are not directly connected with the mooring line are considered to be non-active and of zero projected velocities (namely, mooring line-friction force term S_β^m equals zero). Thus, only the projected velocities for these active control volumes are required to be determined. It should be noted that the definition of active and non-active control volumes in this subsection is primarily aiming for a clear description about the calculation of mooring line friction force for the shallow water flow. All these cells are adopted for solving the governing equations of the shallow water flow using a finite volume method.

Notice that it is not straightforward to calculate the projected velocities for those active control volumes based on the nodal velocities of cable elements for the mooring line system, which is related to the fact that not all active control volumes contain cable nodes (solid dots displayed in Fig. 3). To achieve this goal, a robust projection technique is proposed in the current study. For example, Fig. 4 shows a local computational domain that includes a group of nine control volumes and a representative two-dimensional catenary cable element with end points I and J that intersect with few control volumes. Instead of a direct mapping from cable nodes, each catenary cable segment is considered to be discretized into a number of evenly distributed ghost points (shown by blue squares in Fig. 4) along its length. Since an elastic cable element is adopted here, the cable velocities v^g at these ghost points are determined using a linear interpolation of the cable element nodal velocities v^m. For a specific active cell (displayed as a solid dot in Fig. 4) at the βth layer in the water system, the projected velocities $V_\beta^{m,c}$ of the mooring line are determined by averaging the velocities of all ghost points within the cell domain as

$$V_\beta^{m,c} = \frac{1}{N_g} \sum_{i=1}^{N_g} v^g, \tag{21}$$

where N_g is the total number of ghost points within the domain of a specific control volume. Hence, the friction force term S_β^m for the shallow water flow subjected to a moving mooring line is determined by substituting the Eq. (21) in the system of Eq. (20).

For simplicity in the presentation, the multilayer shallow water Eqs. (1) are reformulated in a compact vector form as

$$\frac{\partial \mathbf{U}}{\partial t} + \frac{\partial \mathbf{F}(\mathbf{U})}{\partial x} = \mathbf{Q}(\mathbf{U}) + \mathbf{R}(\mathbf{U}), \tag{22}$$

where $\mathbf{U}$ is the vector of conserved variables, $\mathbf{F}$ is the vector of flux functions, $\mathbf{Q}$ and $\mathbf{R}$ are vectors of the source terms given by the equations in Box I. Notice that one of the challenges in the numerical solution of the system Eqs. (22) is related to the absence of explicit

$$\mathbf{U} = \begin{pmatrix} H \\ Hu_1 \\ Hu_2 \\ \vdots \\ Hu_N \end{pmatrix}, \qquad \mathbf{F(U)} = \begin{pmatrix} \sum_{\beta=1}^{N} l_\beta Hu_\beta \\ Hu_1^2 + \frac{1}{2}gH^2 \\ Hu_2^2 + \frac{1}{2}gH^2 \\ \vdots \\ Hu_N^2 + \frac{1}{2}gH^2 \end{pmatrix}, \qquad \mathbf{Q(U)} = \begin{pmatrix} 0 \\ -gH\frac{\partial Z}{\partial x} \\ -gH\frac{\partial Z}{\partial x} \\ \vdots \\ -gH\frac{\partial Z}{\partial x} \end{pmatrix},$$

$$\mathbf{R(U)} = \begin{pmatrix} 0 \\ \frac{1}{l_1}\left(u_{3/2}\mathcal{M}_{3/2} + 2\nu\frac{u_2-u_1}{(l_2+l_1)H} - gM_b^2\frac{u_1|u_1|}{H^{1/3}} - \sigma_m^2\rho_w\frac{V_{m,c}|V_{m,c}|}{l_1 H} \right) \\ \frac{1}{l_2}\left(u_{5/2}\mathcal{M}_{5/2} - u_{3/2}\mathcal{M}_{3/2} + 2\nu\frac{u_3-u_2}{(l_3+l_2)H} - 2\nu\frac{u_2-u_1}{(l_2+l_1)H} - \sigma_m^2\rho_w\frac{V_{m,c}|V_{m,c}|}{\sum_{i=1}^{2} l_i H} \right) \\ \vdots \\ \frac{1}{l_{N-1}}\left(u_{N-1/2}\mathcal{M}_{N-1/2} - u_{N-3/2}\mathcal{M}_{N-3/2} + 2\nu\frac{u_{N+1}-u_N}{(l_{N+1}+l_N)H} - 2\nu\frac{u_N-u_{N-1}}{(l_N+l_{N-1})H} - \sigma_m^2\rho_w\frac{V_{m,c}|V_{m,c}|}{\sum_{i=1}^{N-1} l_i H} \right) \\ \frac{1}{l_N}\left(-u_{N-1/2}\mathcal{M}_{N-1/2} - 2\nu\frac{u_N-u_{N-1}}{(l_N+l_{N-1})H} + \sigma_s^2\rho_a\frac{V_{\text{wind}}|V_{\text{wind}}|}{H} - \sigma_m^2\rho_w\frac{V_{m,c}|V_{m,c}|}{\sum_{i=1}^{N} l_i H} \right) \end{pmatrix}.$$
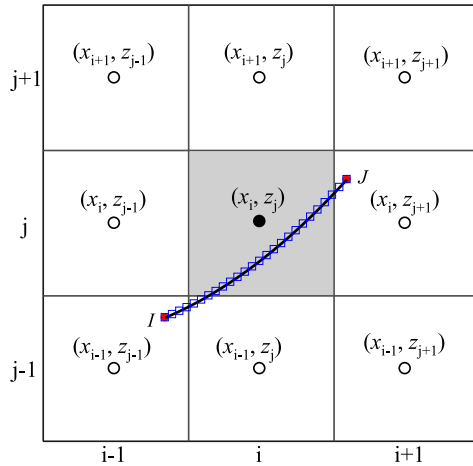
Box I.

Fig. 4. Determination of projected mooring line velocity at control volumes using ghost points.

exact expressions of its eigenvalues which are required in most finite volume methods using the Riemann solvers such as the Roe, HLL, HLLC schemes and other Godunov methods from computational fluids dynamics. However, by assuming that all layered velocities u_β are closed to the mean velocity $\bar{u}$, an asymptotic estimation of these eigenvalues is possible (see for example Audusse et al. (2011b)) for which the first-order approximation of the two barotropic eigenvalues are given by

$$\lambda_{\text{ext}}^{\pm} = u_m \pm \sqrt{g\sum_{\beta=1}^{N} h_\beta} + \mathcal{O}\left(\left| u_\beta - \bar{u} \right|^2 \right), \qquad \text{with} \qquad u_m = \frac{\sum_{\beta=1}^{N} h_\beta u_\beta}{\sum_{\beta=1}^{N} h_\beta}. \quad (23)$$

Similarly, a zeroth-order approximation of the barotropic eigenvalues at the water layer interfaces yields

$$\lambda_{\text{int}}^{\pm,\beta+\frac{1}{2}} = \bar{u} \pm \sqrt{\frac{1}{2}g\sum_{\beta=1}^{N} h_\beta} + \mathcal{O}\left(\left| u_\beta - \bar{u} \right| \right), \qquad \beta = 1, 2, \ldots, N-1. \quad (24)$$

It should be pointed out that Eqs. (23)–(24) are approximations for eigenvalues of the original system using water heights h_β for layers instead of the total height H, which gives a system of $2N$ equations with each water layer having two eigenvalues.

For the numerical solution of the multilayer shallow water model Eqs. (22), the Finite Volume Characteristics (FVC) method proposed in Audusse et al. (2014) is adopted in the current work. The FVC method was first introduced in Benkhaldoun and Seaid (2010) for solving the single-layer shallow water equations and extended in Benkhaldoun et al. (2014) to density-driven shallow water flows. The main feature of the FVC method lies in the fact that it does not use Riemann solvers and therefore, no explicit calculation of eigenvalues for the multilayer system is needed in its formulation. The method is fast, accurate and explicit using the method of characteristics for the time integration. However, the selection of time steps in the FVC method is carried out using the asymptotic approximations Eqs. (23)–(24). In the present work, unlike the previous works (Audusse et al., 2014; Benkhaldoun et al., 2014; Benkhaldoun and Seaid, 2010), the stability of the FVC method is improved by adopting a splitting operator used

for the time integration along with a third-order Runge–Kutta method. Thus, for the spatial discretization of Eq. (22), we discretize the spatial domain into control volumes $[x_{i-1/2}, x_{i+1/2}]$ with non-uniform size $\Delta x_i = x_{i+1/2} - x_{i-1/2}$, $x_{i-1/2} = i\Delta x_i$ and $x_i = (i+1/2)\Delta x_i$ is the centre of the control volume. Integrating Eq. (22) with respect to space over the control volume $[x_{i-1/2}, x_{i+1/2}]$, we obtain the semi-discrete equations

$$\frac{d\mathbf{U}_i}{dt} + \frac{\mathcal{F}_{i+1/2} - \mathcal{F}_{i-1/2}}{\Delta x_i} = \mathbf{Q}(\mathbf{U}_i) + \mathbf{R}(\mathbf{U}_i), \tag{25}$$

where $\mathbf{U}_i(t)$ is the space-averaged approximation of the solution $\mathbf{U}$ in the control volume $[x_{i-1/2}, x_{i+1/2}]$ at time t given by

$$\mathbf{U}_i(t) = \frac{1}{\Delta x_i} \int_{x_{i-1/2}}^{x_{i+1/2}} \mathbf{U}(t, x)\, dx,$$

and $\mathcal{F}_{i\pm1/2} = \mathbf{F}(\mathbf{U}_{i\pm1/2})$ are the numerical fluxes at the cell interfaces $x = x_{i\pm1/2}$ and time t to be reconstructed in each control volume. For the time integration of Eq. (25), we divide the time interval into sub-intervals $[t_n, t_{n+1}]$ with a length $\Delta t_n = t_{n+1} - t_n$. We also use the notation W^n to denote the value of a generic function W at time t_n. Hence, the splitting operator consists of the following three steps:

Step 1:

$$\frac{d\mathbf{U}_i^*}{dt} = \mathbf{R}(\mathbf{U}_i^*), \qquad t \in (t_n, t_{n+1}],$$

$$\tag{26}$$

$$\mathbf{U}_i^*(t_n) = \mathbf{U}_i(t_n).$$

Step 2:

$$\frac{d\mathbf{U}_i^{**}}{dt} + \frac{\mathcal{F}_{i+1/2}^{**} - \mathcal{F}_{i-1/2}^{**}}{\Delta x_i} = \mathbf{Q}(\mathbf{U}_i^{**}), \qquad t \in (t_n, t_{n+1}],$$

$$\tag{27}$$

$$\mathbf{U}_i^{**}(t_n) = \mathbf{U}_i^*(t_n).$$

Step 3:

$$\frac{d\mathbf{U}_i^{***}}{dt} = \mathbf{R}(\mathbf{U}_i^{***}), \qquad t \in (t_n, t_{n+1}],$$

$$\tag{28}$$

$$\mathbf{U}_i^{***}(t_n) = \mathbf{U}_i^{**}(t_{n+1}).$$

In Eq. (27), the numerical fluxes are $\mathcal{F}_{i\pm1/2}^{**} = \mathbf{F}(\mathbf{U}_{i\pm1/2}^{**})$. To complete the time integration, the explicit third-order Runge–Kutta scheme investigated in Amiri et al. (2013) is used for the three steps Eqs. (26)–(28). Thus, to advance the solution of an ordinary differential equation of the form Eq. (26), the Runge–Kutta scheme is carried out as

$$\mathcal{U}_i^{(1)} = \mathbf{U}_i^n + \Delta t_n \mathbf{R}(\mathbf{U}_i^n),$$
$$\mathcal{U}_i^{(2)} = \frac{3}{4}\mathbf{U}_i^n + \frac{1}{4}\mathcal{U}_i^{(1)} + \frac{1}{4}\Delta t_n \mathbf{R}(\mathcal{U}_i^{(1)}), \tag{29}$$
$$\mathbf{U}_i^{n+1} = \frac{1}{3}\mathbf{U}_i^n + \frac{2}{3}\mathcal{U}_i^{(2)} + \frac{2}{3}\Delta t_n \mathbf{R}(\mathcal{U}_i^{(2)}),$$

where we have dropped the asterisk from the variables in Eq. (26) for ease of notation. Note that the Runge–Kutta method Eqs. (29) is a convex combination of first-order Euler steps which exhibits strong stability properties and it has been widely used for time integration of hyperbolic systems of conservation laws. It is also clear that using the time stepping scheme in Eqs. (29), no nonlinear or linear systems of algebraic equations are needed to be solved. In addition, the scheme Eqs. (29) is TVD, third-order accurate in time, and stable under the standard Courant–Friedrichs–Lewy (CFL) condition

$$\Delta t_n \leq \min_i \left(\frac{\Delta x_i}{\max_\beta \left(\left| \lambda_{\text{ext},i}^{\pm,n} \right|, \left| \lambda_{\text{int},i}^{\pm,\beta+\frac{1}{2},n} \right| \right)} \right), \tag{30}$$

where $\lambda_{\text{ext},i}^{\pm,n}$ and $\lambda_{\text{int},i}^{\pm,\beta+\frac{1}{2},n}$ are the asymptotic eigenvalues defined in Eqs. (23) and (24), respectively. In the current study, we use the FVC reconstruction for the approximation of numerical fluxes $\mathcal{F}_{i\pm1/2}$ and the well-balanced discretization for source terms $\mathbf{Q}(\mathbf{U}_i)$ and $\mathbf{R}(\mathbf{U}_i)$ in Eq. (25). Details on these techniques can be found in Audusse et al. (2014) and are not repeated here for brevity in the presentation.

Once the water velocities u_β are computed for each βth layer, we generate the two-dimensional velocity fields from these one-dimensional results using the post-processing procedure studied in Audusse et al. (2014). Thus, the vertical velocity w is obtained using the divergence-free equation

$$\frac{\partial u}{\partial x} + \frac{\partial w}{\partial z} = 0. \tag{31}$$

Hence, integrating Eq. (31) over a control volume $[x_{i-1/2}, x_{i+1/2}] \times [h_{\beta-1/2}, h_{\beta+1/2}]$ we obtain

$$w_{\beta,i}^n = w_{\beta-1,i} + \Delta z_\beta^n \left(\frac{u_{\beta,i+1/2}^n - u_{\beta,i-1/2}^n}{\Delta x_i} \right), \qquad \beta = 2, 3, \ldots, N,$$

where $\Delta z_\beta^n = \frac{h_{\beta+1} + h_\beta}{2}$ is the vertical step between two layers. Here, on the bottom boundary we use non-penetration boundary conditions.

3.2. Numerical solution of the mooring lines in the fully coupled system

When considering a fully coupled dynamic water-mooring line system, the effects of shallow water flows on the dynamic motion of the mooring line system is considered by including a current force term in the governing equations. In this study, components of the external force that govern the dynamic motion of the submerged mooring line system are composed of the weight $\mathbf{W}$, buoyancy $\mathbf{B}$, current force $\mathbf{F}^c$, seabed reaction force $\mathbf{F}^r$, seabed damping force $\mathbf{F}^d$, and seabed friction force $\mathbf{F}^f$. For instance, the nodal force $\mathbf{W}_I$ at the node I shared by the mooring segments m and $m+1$ is computed as

$$\mathbf{W}_I = \frac{1}{2}\sum_{k=m}^{m+1} \left(\mathbf{B}_k - \mathbf{W}_k\right) = \frac{1}{2}\sum_{k=m}^{m+1} \left(\rho_w - \rho\right) g A_k l_k, \tag{32}$$

where subscript k defines the kth mooring segment, $\mathbf{B}_k$ and $\mathbf{W}_k$ are respectively, the buoyancy and weight of kth mooring segment with its cross-sectional area and (unstrained) length being defined by A_k and l_k, respectively.

Similar to the influence of the shallow water flows on the motion of mooring line, the semi-empirical Morison equation (Sarpkaya, 1986; Sumer et al., 2006) is widely used in computational fluid dynamics to estimate the current force $\mathbf{F}^c$ acting on a moving body in a flow system (Gudmestad and Moe, 1996; Veritas, 2005). This includes contributions of the Froude–Krylov force, the hydrodynamic mass force, and the viscous drag force. For this purpose, this equation is also adopted in the present study for determining the current force on the mooring line owing to the flow field of the shallow water system. Assuming a shallow water flow with a velocity $\dot{u}_w$, the current force $\mathbf{F}^c$ per unit length acting on the mooring line is calculated following the Morison's equation as

$$\mathbf{F}^c = \mathbf{F}^{c,\tau} + \mathbf{F}^{c,\nu},$$

$$= \rho_w V \ddot{u}_w^\tau + C_a^\tau \rho_w V \left(\ddot{u}_w^\tau - \ddot{u}_m^\tau\right) + \frac{1}{2}C_d^\tau \rho_w D (\dot{u}_w^\tau - \dot{u}_m^\tau)\left|\dot{u}_w^\tau - \dot{u}_m^\tau\right|, \quad (33)$$

$$= \rho_w V \ddot{u}_w^\nu + C_a^\nu \rho_w V \left(\ddot{u}_w^\nu - \ddot{u}_m^\nu\right) + \frac{1}{2}C_d^\nu \rho_w D (\dot{u}_w^\nu - \dot{u}_m^\nu)\left|\dot{u}_w^\nu - \dot{u}_m^\nu\right|,$$

where the subscripts w and m define respectively, variables related to the shallow water flow and the mooring system, ρ_w is the water density, $V = \frac{\pi}{4}D^2$ is the mooring line volume per unit length, with D is the diameter of the mooring line, $\ddot{u}_w$ and $\dot{u}_w$ are the acceleration and velocity of water flow, $\ddot{u}_m$ and $\dot{u}_m$ are the acceleration and velocity of the mooring line, which are the time derivatives of its displacement u_m. In Eq. (33), C_a and C_d are the added mass and drag force coefficients.
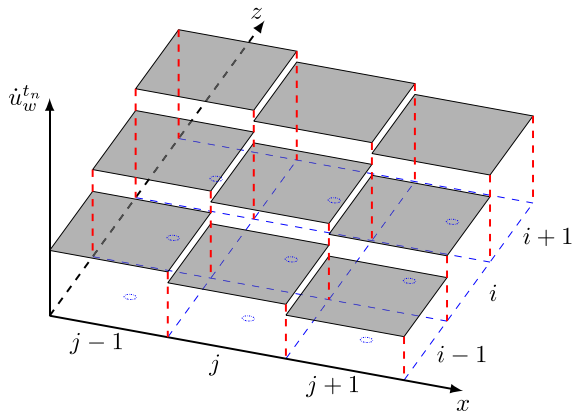
Fig. 5. Schematic diagram of discontinuous velocity fields along x-direction for finite volume cells.
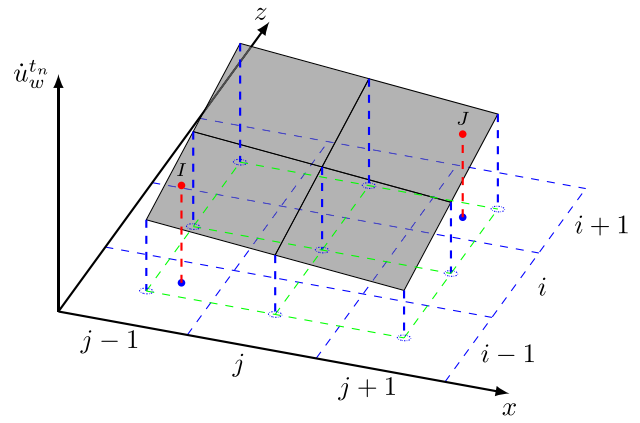

Fig. 6. Reconstructed continuous velocity fields along the x-direction for finite volume cells based on a MLSA scheme.

It should be pointed out that, when using Eq. (33) to evaluate the nodal current force for the mooring line system, the shallow water velocities at the nodes of catenary elements should be determined.

Note that, because the mooring line system is discretized into a group of catenary cable elements, the current force acting on a specific catenary element is calculated by first evaluating the nodal incline force at the two end points and then, a linear interpolation is used for the whole element. However, when using the FVC solver for the multilayer shallow water equations, the depth-averaged velocities and accelerations are computed at the centres of finite volume cells, which are generally discontinuous at the cell edges. For instance, Fig. 5 depicts the water velocity fields $\dot{u}_w^{t_n}$ along the x-direction for a group of nine cells at time t_n. Similar discontinuities are also expected for the water acceleration fields. Owing to dynamic motion of the mooring line, nodes of the catenary cable elements may move from one cell to another. Therefore, when using Eq. (33) to determine the current forces acting on the mooring line, these discontinuities in both acceleration and velocity fields can lead to undesired oscillations in the calculated forces and thus, resulting in a nonphysical vibration of the mooring system. To alleviate such nonphysical oscillations, an improved interpolation scheme for mapping velocities and accelerations from cell centres to catenary element nodes is required. Following the ideas reported in Zienkiewicz and Zhu (1992a), a linear patch recovery based on a Moving Least Squares Approximation (MLSA) for interpolating velocities and accelerations is proposed in this study, which is also similar to the one adopted in Zheng et al. (2021). As shown in Fig. 6, a patch of four neighbouring finite volume cells (two cells along each direction) can be identified. Here, within such a patch, a quadrilateral area which is bounded by green dashed lines in Fig. 6 can be defined by using the central points of the four neighbouring cells. For the interpolation of velocities and accelerations, a polynomial approximation of order p in the considered quadrilateral area is then introduced. Here, the approximation for the interpolated water velocity at time t_n is defined by

$$\dot{u}_w^{t_n}(x, z) = \boldsymbol{Q}(x, z)\boldsymbol{a}, \tag{34}$$

where (x, z) are coordinates of the centre points of finite volume cells in the quadrilateral area, $\boldsymbol{Q}$ and $\boldsymbol{a}$ are vectors containing polynomial basis functions and interpolation degrees-of-freedom, respectively. Similar treatments are also applied for interpolation of the acceleration and it is therefore omitted for the purpose of simplification.

In general, different basis functions may be chosen to approximate both velocity and acceleration variables. In this study, a linear version of $\boldsymbol{Q}(x_i, z_i) = \begin{pmatrix} 1 & x_i & z_i & x_i z_i \end{pmatrix}^\top$ is chosen, which leads after determination of the coefficients $\boldsymbol{a} = \begin{pmatrix} a_0 & a_1 & a_2 & a_3 \end{pmatrix}^\top$, to a linear interpolation plane shown in Fig. 6. Note that based on a *posteriori* error estimator, the

relative error $E(\boldsymbol{a})$ of the interpolated velocities at the centres of finite volume cells is calculated as

$$E(\boldsymbol{a}) = \sum_{i=1}^{N_c} \left(\dot{u}_w^{t_n}(x_i, z_i) - \boldsymbol{Q}(x_i, z_i)\boldsymbol{a} \right)^2, \tag{35}$$

where N_c is the total number of finite volume cells in the approximation domain, and (x_i, z_i) are the coordinates of the centre points of the cells. It should also be stressed that, minimizing the error with respect to $\boldsymbol{a}$ requires the solution of a linear system as

$$\boldsymbol{A}\boldsymbol{a} = \boldsymbol{b}, \tag{36}$$

with $\boldsymbol{A} = \sum_{i=1}^{N_{cp}} \boldsymbol{Q}^\mathrm{T}(x_i, z_i)\boldsymbol{Q}(x_i, z_i)$ and $\boldsymbol{b} = \sum_{i=1}^{N_{cp}} \boldsymbol{Q}^\mathrm{T}(x_i, z_i)\dot{u}_w^{t_n}(x_i, z_i)$. After solving the above linear system, the interpolated velocities $\dot{u}_{w,I}^{t_n}$ at the Ith catenary element node of the mooring line located in the computational domain is computed using

$$\dot{u}_{w,I}^{t_n}\left(x_m^I, z_m^I\right) = \boldsymbol{Q}\left(x_m^I, z_m^I\right)\boldsymbol{a}, \tag{37}$$

where $\left(x_m^I, z_m^I\right)$ are coordinates of the Ith node of the mooring line in the quadrilateral area. As discussed in Zheng et al. (2021), for those catenary element nodes located near the domain boundary, there might be insufficient finite volume cells to form a complete patch. In these cases, the water velocities and accelerations at the catenary element nodes are determined by extending internal patches up to the position of these nodes. Similar ideas have been implemented for determining variables at boundary nodes in the finite element methods, see for example Zienkiewicz and Zhu (1992a,b) and Zienkiewicz et al. (2005). Once the water velocities and accelerations at the catenary element nodes are calculated, the current nodal force $\boldsymbol{F}_I^c$ of the mooring line can be readily evaluated.

It should be stressed that another main contribution of external forces for the mooring line system that should be addressed is the mooring line-seabed interaction force. In some previous studies, the spring–damper model in the mooring system is frequently adopted to control the interactions between the mooring line and the seabed, see for example Li and Choung (2021a), Low et al. (2018), Webster (1995) and Gobat and Grosenbaugh (2006). In a similar manner, the seabed reaction force $\boldsymbol{F}^r$, seabed damping force $\boldsymbol{F}^d$, and seabed friction force $\boldsymbol{F}^f$ between the node I of mooring line and the seabed are computed as

$$\boldsymbol{F}_I^r = K_b\left(z_s - z_I\right) \sum_{i=k}^{k+1} \frac{D_i l_i}{2},$$

$$\boldsymbol{F}_I^v = C_b \sum_{i=k}^{k+1} \frac{D_i l_i}{2} \dot{u}_{m,I}^v, \tag{38}$$

$$\boldsymbol{F}_I^f = C_f D_f \dot{u}_{m,I}^\tau,$$

where K_b is the contact seabed stiffness per unit area, z_s the reference elevation and it is usually the same as seabed elevation, z_I the elevation of the catenary element node, D_i the diameter of the ith catenary segment of mooring line, C_b the seabed damping coefficient per unit area, C_f the seabed friction coefficient, and D_f the seabed friction damping coefficient. Note that the seabed reaction force $\boldsymbol{F}_I^r$ is active only when the nodal elevation z_I is smaller than z_s. In addition, the seabed damping force $\boldsymbol{F}_I^v$ becomes non-zero only when the node I moves downward and the seabed reaction force does not vanish.

Once the nodal contact forces are computed, the full set of governing equations for the dynamic motion of the mooring line can be reformulated in a compact form as

$$\mathbf{K}\boldsymbol{u} + \mathbf{C}\dot{\boldsymbol{u}} + \mathbf{M}\ddot{\boldsymbol{u}} = \boldsymbol{F}, \tag{39}$$

where $\mathbf{K}$ is the global tangent stiffness matrix, $\mathbf{M}$ the global mass matrix, $\mathbf{C} = \mu\mathbf{M} + \lambda\mathbf{K}$ the global Rayleigh damping matrix, with μ and λ are respectively, the mass and stiffness proportional damping coefficients, and $\boldsymbol{F}$ is the time-varying external force vector accounting for all forces as $\boldsymbol{F} = \boldsymbol{W} + \boldsymbol{F}^c + \boldsymbol{F}^r + \boldsymbol{F}^v + \boldsymbol{F}^f$.

The time integration of Eq. (39) is performed using the well-established Newmark algorithm (Newmark, 1959). Thus, in compliance with Newmark's time integration, the following recurrence relationships for stepping from current time t_n to the next time t_{n+1} using two integration parameters γ and β are obtained

$$\ddot{\boldsymbol{u}}_{n+1} = \ddot{\boldsymbol{u}}_n + \Delta t_n \dddot{\boldsymbol{u}}, \tag{40a}$$

$$\dot{\boldsymbol{u}}_{n+1} = \dot{\boldsymbol{u}}_n + \Delta t_n\big((1-\gamma)\ddot{\boldsymbol{u}}_n + \gamma\ddot{\boldsymbol{u}}_{n+1}\big), \tag{40b}$$

$$\boldsymbol{u}_{n+1} = \boldsymbol{u}_n + \dot{\boldsymbol{u}}_n\Delta t_n + \frac{\Delta t_n^2}{2}\big((1-2\beta)\ddot{\boldsymbol{u}}_n + 2\beta\ddot{\boldsymbol{u}}_{n+1}\big), \tag{40c}$$

with $\Delta t_n = t_{n+1} - t_n$ is the time step. It is worth mentioning that the governing equations for the mooring line is solved implicitly in time, thus the choice of time step Δt_n for the coupled system should only satisfy the CFL condition required by the FVC method. Substituting Eq. (40c) into Eqs. (40a) and (40b), the recurrence relations for the acceleration $\ddot{\boldsymbol{u}}_{n+1}$ and velocity $\dot{\boldsymbol{u}}_{n+1}$ can be reformulated as

$$\ddot{\boldsymbol{u}}_{n+1} = \frac{1}{\beta\Delta t_n^2}\big(\boldsymbol{u}_{n+1} - \boldsymbol{u}_n\big) - \frac{1}{\beta\Delta t_n}\boldsymbol{v}_n - \Big(\frac{1}{2\beta}-1\Big)\ddot{\boldsymbol{u}}_n, \tag{41a}$$

$$\dot{\boldsymbol{u}}_{n+1} = \frac{\gamma}{\beta\Delta t_n}\big(\boldsymbol{u}_{n+1} - \boldsymbol{u}_n\big) - \Big(\frac{\gamma}{\beta}-1\Big)\dot{\boldsymbol{u}}_n - \Big(\frac{\gamma}{2\beta}-1\Big)\Delta t_n\ddot{\boldsymbol{u}}_n. \tag{41b}$$

Note that, in the case of linear elastodynamics, the Newmark time integration is unconditionally stable, non-dissipative, and second-order accurate when $\beta = 0.25$ and $\gamma = 0.5$, which is the sole parameter pair considered in this study. Here, after substituting Eqs. (41a) and (41b) into Eq. (39), the final algebraic system of the fully discretized equations is

$$\overline{\mathbf{K}}\Delta\boldsymbol{u}_{n+1} = \boldsymbol{F}_{n+1} - \boldsymbol{F}_n^{\text{int}} + \mathbf{M}_n\left(\frac{1}{\beta\Delta t_n}\dot{\boldsymbol{u}}_n + \Big(\frac{1}{2\beta}-1\Big)\ddot{\boldsymbol{u}}_n\right)$$
$$+ \mathbf{C}_n\left(\Big(\frac{\gamma}{\beta}-1\Big)\dot{\boldsymbol{u}}_n + \Big(\frac{\gamma}{2\beta}-1\Big)\ddot{\boldsymbol{u}}_n\Delta t_n\right), \tag{42}$$

where $\overline{\mathbf{K}} = \frac{1}{\beta\Delta t_n^2}\mathbf{M}_n + \frac{\gamma}{\beta\Delta t_n}\mathbf{C}_n + \mathbf{K}_n$ is the effective stiffness matrix. Note that the above system is intrinsically nonlinear and it must be solved in an iterative manner. For this purpose, each step in Eq. (42) is solved in combination with a well-established Newton–Raphson iteration scheme (Zienkiewicz et al., 2005). A convergent solution for $\Delta\boldsymbol{u}_{n+1}$ is obtained when the residual unbalance force vector $\boldsymbol{R}^k$ (*i.e.* the right side of Eq. (42)) meets the following criterion

$$\frac{\left\|\boldsymbol{R}^k\right\|}{\left\|\boldsymbol{R}^0\right\|} \le tol, \tag{43}$$

where the superscript k refers to the Newton iteration counter, and tol is a prescribed tolerance set to 10^{-8} in our simulations. When

the convergence is reached according to the prescribed tolerance, all relevant variables for the mooring line system are updated.

In summary, details regarding the coupled solution algorithm for the numerical implementation of the fully dynamic coupled system proposed in the current work are summarized in Fig. 7. Here, for each considered step, the dynamic motion of the fully coupled water-mooring line system is explicitly solved according to the following sequence of sub-steps:

(1) Initialize material parameters and state variables for the shallow water system and mooring line system.
(2) Compute the eigenvalues $\lambda_{\text{ext}}^{\pm}$ and $\lambda_{\text{int}}^{\pm,\beta+\frac{1}{2}}$ using Eqs. (23) and Eq. (24), and adjust the time step according to the stability condition Eq. (30).
(3) Reconstruct the source terms $\mathbf{Q}(\mathbf{U})$ and $\mathbf{R}(\mathbf{U})$ as defined in Eq. (22).
(4) For each control volume $[x_{i-1/2}, x_{i+1/2}]$, compute the numerical fluxes $\mathcal{F}_{i+1/2}$ using the FVC method as described in Audusse et al. (2014).
(5) Solve the first step (26) of the splitting procedure using the Runge–Kutta scheme Eq. (29).
(6) Solve the second step (27) of the splitting procedure using the Runge–Kutta scheme Eq. (29).
(7) Solve the third step (28) of the splitting procedure using the Runge–Kutta scheme Eq. (29).
(8) Compute the local stiffness matrices $\mathbf{k}_n$, mass matrices $\mathbf{m}_n$, and damping matrices $\mathbf{c}_n$ for each catenary cable element.
(9) Assemble the global stiffness matrices ($\mathbf{K}_n$, $\mathbf{M}_n$, and $\mathbf{C}_n$) and calculate the effective stiffness matrix $\overline{\mathbf{K}}$ using Eq. (42).
(10) Calculate the global loading vectors $\boldsymbol{F}$ using Eq. (38) with incorporating the influence of the current force from shallow water system $\boldsymbol{F}^c$ in Eq. (33).
(11) Solve the nonlinear governing equation of the mooring line system using the Newton–Raphson iterations and update unbalanced force vectors using Eq. (42).
(12) Check the convergence of the dynamic mooring line system using Eq. (43).
(13) Update the positions of mooring line using Eq. (40c) and other related state variables (e.g., Eqs. (40a) and (40b)) for the solution of the next calculation step.

It should be stressed that, in the proposed fully coupled dynamic water-mooring line system, the frictional source terms are included in each layer of the water domain for modelling the interaction between the shallow water flow and the submerged mooring line system, while the numerical simulation of nonlinear dynamics of the mooring line is carried out using a group of elastic catenary cable elements for space discretization and an implicit scheme using the Newton's iterations for the time integration with the inclusion of water current forces which account for the influence of shallow water on the mooring line.

4. Numerical results and applications

In this section, we first present a class of verification examples for the multilayer shallow water flows and the nonlinear analysis of cable systems to examine the accuracy of the proposed methods. It should be pointed out that owing to the fact that very limited experimental data are reported to include those dynamic interaction effects in the complex coupled system, it is difficult to validate the fully coupled system through comparison with the experimental measurements. For this reason, we have considered several numerical examples to separately validate the suitability of the multilayer finite volume solver for capturing the shallow water flows and the fully dynamic nonlinear catenary cable element for reproducing the dynamic motion of the mooring line system. The second class of numerical results aim to demonstrate
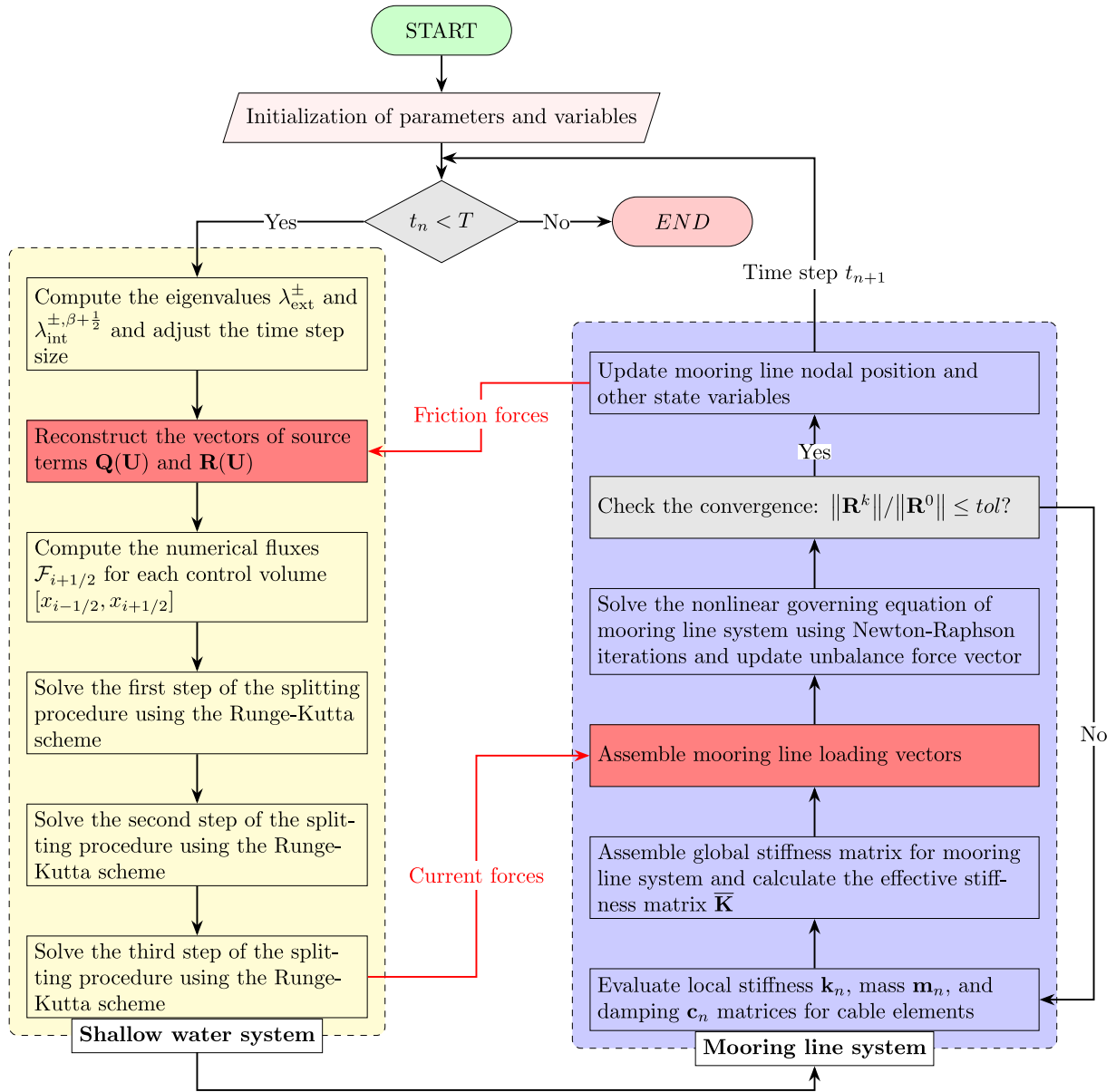
Fig. 7. Dynamic coupled algorithm for the multilayer shallow water-mooring line system.

the computational performance of the fully coupled shallow water-mooring line system using two examples for wind-driven flows over flat and non-flat beds. For all results presented in this section, we assume that the total water height H and the total number of layers N are given whereas, the water height h_β at each βth layer is equidistantly calculated as

$$h_\beta = l_\beta H, \qquad \text{with} \qquad l_\beta = \frac{1}{N}, \qquad \beta = 1, 2, \dots, N.$$

In all results presented in this section, the Courant number is set to $C_r = 0.75$ in all the examples and the time stepsize Δt_n is adjusted at each step according to the CFL condition Eq. (30) as

$$\Delta t_n = C_r \min_i \left(\frac{\Delta x_i}{\max\limits_{1 \leq \beta \leq N-1} \left(\left| \lambda_{\text{ext}}^+ \right|, \left| \lambda_{\text{ext}}^- \right|, \left| \lambda_{\text{int}}^{+, \beta + \frac{1}{2}} \right|, \left| \lambda_{\text{int}}^{-, \beta + \frac{1}{2}} \right| \right)} \right),$$

where $\lambda_{\text{ext}}^\pm$ and $\lambda_{\text{int}}^{\pm, \beta + \frac{1}{2}}$ are the approximated eigenvalues in Eqs. (23) and (24), respectively. The following examples are selected:

4.1. Verification of the multilayer finite volume solver for a dam-break problem

First we verify the performance of the finite volume method for solving multilayer shallow water flows generated by a dam-break problem over a flat bed. Here, we compare the numerical results obtained using the FVC method for multilayer shallow water systems with 5 and 20 layers to the experimental results reported in Liu et al. (2018). To this end, we consider the same benchmark set-up as described in Liu et al. (2018) for a dam breaks over a flat frictionless bed flume 19 m long with no wind effects. The initial conditions for the water height and velocities are given by

$$H(0, x) = \begin{cases} 0.60 \, \text{m}, & \text{if} \quad x \leq 0, \\ 0.24 \, \text{m}, & \text{if} \quad x > 0, \end{cases} \qquad u_\beta(0, x) = 0 \, \text{m/s}.$$

In our simulations, the vertical kinematic eddy viscosity $\nu = 0.001 \, \text{m}^2/\text{s}$, the domain is discretized into 190 control volumes and results are presented at the final time $t = 3.5 \, \text{s}$. Fig. 8 depicts the obtained
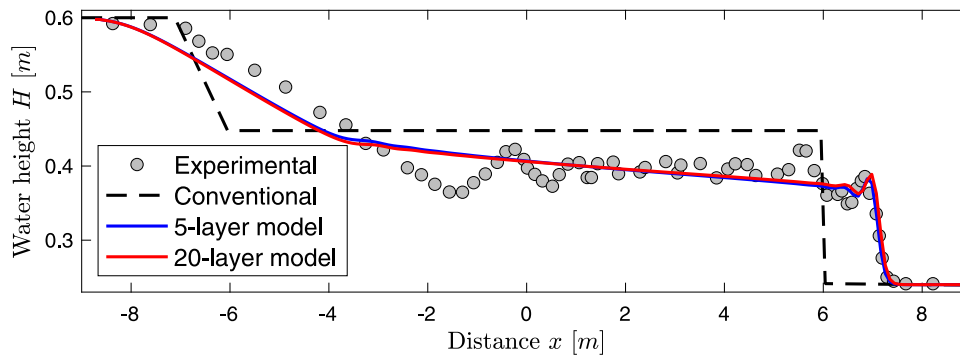
Fig. 8. Comparison between experimental measurements and computational results obtained for the dam-break problem over a fixed bed at time $t = 3.5$ s using different numbers of layers.

numerical results for the water height along with the experimental measurements from (Liu et al., 2018). For comparison, numerical results obtained using the conventional single-layer shallow water equations are also included in Fig. 8. It is clear that the numerical results obtained using the multilayer shallow water system are in good agreement with the experimental measurements for this dam-break problem. The conventional single-layer model widely used in literature to model shallow water flows fails to resolve this problem, compare the location of the shock and rarefaction waves in Fig. 8. The high accuracy of the FVC method solving this benchmark problem is also demonstrated in these numerical results. Fig. 8 also confirms the advantage of the multilayer formulation of shallow water flows and the effect of numbers of layers in the computed results. For instance, it is evident from the results displayed in Fig. 8 that more accurate results are obtained by increasing the number of layers in the multilayer system for this dam-break problem. For the considered flow conditions, using the 5-layer model yields an L^2-error (between numerical and experimental results) of 0.1933 whereas, using the 20-layer model this error becomes 0.1732. It should also be stressed that although this improvement in the accuracy is relatively small, it will become critical when evaluating fully coupled shallow water-mooring line systems as the water depth and velocity field would be sensitive to the dynamics present in the model.

4.2. Verification of the multilayer finite volume solver for a wind-driven recirculation flow

Our next concern is to examine the numerical performance of the FVC method for solving wind-driven recirculation flow problems using the multilayer shallow water equations Eqs. (1). To this end, we consider a test example of wind-driven recirculation flows in a long water channel with flat topography studied in Audusse et al. (2011b, 2014) and Izem and Seaid (2021) among others. Note that this example has been widely used in the literature because analytical velocity profiles are available in Shankar et al. (1997). Hence, we use the same parameters as in Shankar et al. (1997) and solve the system of Eq. (22) in a flat rectangular channel of $3400 \times 1400 \times 10$ m subject to a uniform wind stress of $\sigma = 1.5$ N/m^2 applied at the surface, equivalent to a wind speed of $V_{wind} = 28.83$ m/s blowing from the left of the channel. As in Shankar et al. (1997), the viscosity coefficient $\nu = 100$ cm^2/s, the Manning's roughness coefficient $M_b = 0.1$ cm/s, the wind stress coefficient $\sigma_s^2 = 0.0015$, the water density $\rho = 1025$ kg/m^3, the air density $\rho_a = 1.2$ kg/m^3 and the gravity $g = 9.81$ m/s^2. Using no-slip conditions, it has been shown in Shankar et al. (1997) that at a given elevation $z \in [-10, 0]$ an analytical solution of the velocity can be derived as

$$u(z) = \frac{\sigma}{\rho \nu H}\left(\frac{3}{4}z^2 + Hz + \frac{1}{4}H^2\right). \tag{44}$$

Note that the velocity profile in Eq. (44) is a parabola with two zeros attained at $z = -H$ and $z = -\frac{H}{3}$ whereas, the minimum and maximum vertical velocities are $\frac{-1}{12}\frac{\sigma H}{\rho \nu}$ and $\frac{1}{4}\frac{\sigma H}{\rho \nu}$, respectively. In Fig. 9 we present the velocity profiles at the channel centre $x = 1700$ m at time $t = 20$ s using 170 control volumes for 5-layer, 10-layer and 20-layers models. For comparison reasons, the exact velocity profile and results obtained for the three-dimensional system using the TELEMAC-3D.[1] software are also presented in Fig. 9 Notice that the three-dimensional simulations on TELEMAC-3D are carried out on a structured mesh of 25 600 elements and 15 015 nodes using a fixed time step $\Delta t = 1.0$ s. It is clear from the obtained results that, under the actual wind and flow conditions, the FVC method accurately solves this problem and the computed solutions compare very well with the exact solution. It is also evident that an increase in the number of layers in the shallow water model results in an excellent convergence to the analytical solution. The computational results obtained using the multilayer shallow water systems are also in good agreement with those obtained using the three-dimensional model. Overall, the numerical results obtained for this wind-driven recirculation flow problem demonstrate the ability of the FVC method to resolve the small flow features within the channel without generating spurious oscillations. For instance, a simple inspection of these results confirm that the vertical velocity profiles are accurately captured by the finite volume method. In addition, for the considered flow conditions, the computational cost for the three-dimensional simulation using TELEMAC-3D is more than 235, 110 and 53 times higher than the simulations obtained using 5-layer, 10-layer and 20-layers models, respectively. This confirms the high efficiency of the proposed multilayer shallow water model and the finite volume solver adopted in the present study.

4.3. Verification of nonlinear quasi-static analysis of a cable system

To illustrate the capability of the adopted catenary cable elements, the quasi-static nonlinear analysis of an isolated cable under a static concentrated load, which has been previously studied (Michalos and Birnstiel, 1962; O'Brien and Francis, 1965; Jayaraman and Knudson, 1981; Tibert, 1998; Andreu et al., 2006; Yang and Tsay, 2007; Thai and Kim, 2011; Abad et al., 2013), is investigated in this study. As shown in Fig. 10, the isolated cable has a span of 304.8 m, a mid-span sag of 30.48 m, and it is supported by two end points (1 and 3) located at the same elevation. A concentrated load of 35.586 kN is applied at the point 2, and its initial distance from point 1 is 121.92 m. The considered material and geometrical properties of the cable are listed in Table 1.

Table 2 compares the calculated displacements at point 2 of the isolated cable from the present study and those from previous studies,
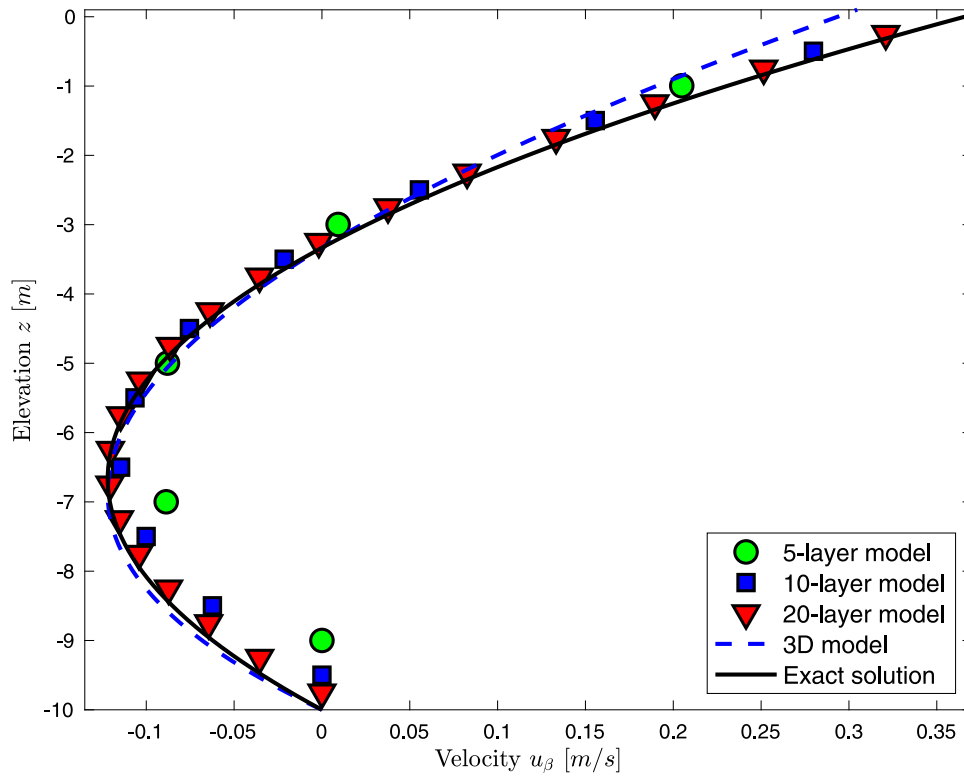
---

[1] http://wiki.opentelemac.org/.

Fig. 9. Comparison between numerical results and the analytical solution obtained for the wind-driven circulation flow problem at time $t = 20\,\mathrm{s}$ using different numbers of layers.
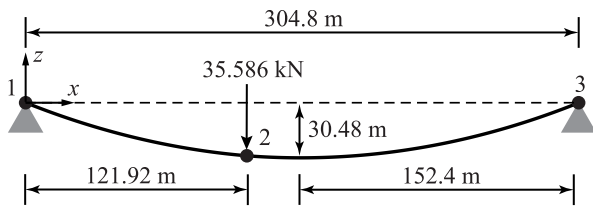

Fig. 10. An isolated cable under the concentrated load of $35.586\,\mathrm{kN}$ at point 2.

Table 1
Material and geometrical properties of an isolated cable under the concentrated load.

Variable	Symbol	Value
Cross-sectional area	A	5.484 cm^2
Elastic modulus	E	13 100.0 kN/cm^2
Cable self-weight	w_3	46.12 N/m
Sag under self-weight at load point	s	29.276 m
Unstressed cable length of sections 1–2	L_0^1	125.88 m
Unstressed cable length of sections 2–3	L_0^2	186.85 m

and an excellent match can be readily observed. In addition, it can be concluded that the elastic catenary elements adopted in this study, generally provide slightly larger displacements owing to its more deformable property compared to those results reported in Thai and Kim (2011). This comparison demonstrates the capability of the adopted catenary cable elements in capturing the nonlinear motion of the cable system.

4.4. Verification of nonlinear dynamic analysis of an inclined cable subjected to an earthquake loading

As a further verification for the dynamic behaviour of the cable system, nonlinear motion of an inclined cable subjected to an earthquake loading reported in Thai and Kim (2011) is investigated and

it is shown in Fig. 11. Here, Fig. 11(a) displays the schematic model for an inclined cable with the presence of an earthquake loading. The inclined cable is composed of two segments with a lumped mass of $m = 1.0\,\mathrm{N\,s^2/mm}$ located at the centre of the cable. Each cable has an initial unstressed length $l_u = 4.995\,\mathrm{m}$, a projected horizontal length $l = 4.0\,\mathrm{m}$, and a projected vertical length $h = 3.0\,\mathrm{m}$. The associated cable properties include the cross-sectional area $A = 100\,\mathrm{mm}^2$ and the elastic modulus $E = 200\,\mathrm{GPa}$. For the purpose of comparison, the self-weight of the cable system is not considered (*i.e.* $w = 0$), while the earthquake record of the EI Centro (as shown in Fig. 11(b)) is chosen as the ground excitation that activates the dynamic motion of the cable system. Fig. 12 illustrates the time evolution of the horizontal displacement u_x for the centre point of the inclined cable under the influence of the earthquake record of EI Centro obtained using the proposed method. It can be concluded that the proposed nonlinear dynamic solutions are in good agreement with those published in Thai and Kim (2011) (despite not included in this study). Here, Table 3 compares the peak displacement responses in both horizontal and vertical directions from the present study with those presented in Thai and Kim (2011), the excellent match further demonstrates the robustness of the adopted elastic catenary element and the accuracy of the present numerical implementation.

### 4.5. Multilayer wind-driven shallow water-cable system on a flat bottom

To illustrate the computational performance of the proposed fully coupled shallow water-mooring line system, the wind-driven flow of multilayer shallow water and dynamic motion of mooring lines in a rectangular flat channel are first investigated. The schematic diagram of the computational model is shown in Fig. 13(a). Here, a wind blows from the left-hand side of the domain with a speed of $V_{\mathrm{wind}} = 20\,\mathrm{m/s}$. The flat channel has a length of $x = 100\,\mathrm{m}$ and it is filled by the water with an initial depth of $H = 10\,\mathrm{m}$. The density $\rho_w = 1000\,\mathrm{kg/m}^3$, the viscosity coefficient $\nu = 0.1\,\mathrm{m^2/s}$, the friction coefficient $\kappa = 1 \times 10^{-5}\,\mathrm{m/s}$, the wind stress coefficient $\sigma_s^2 = 1.5 \times 10^{-3}$, and the

Table 2
Comparison of displacements at point 2 for an isolated cable under the concentrated load.

| Study	Element type	Vertical displacement (m)	Horizontal displacement (m)
Michalos and Birnstiel (1962)	Elastic straight	−5.472	−0.845
O'Brien and Francis (1965)	Elastic catenary	−5.627	−0.860
Jayaraman and Knudson (1981)	Elastic straight	−5.471	−0.845
Jayaraman and Knudson (1981)	Elastic catenary	−5.626	−0.859
Tibert (1998)	Elastic catenary	−5.626	−0.859
Andreu et al. (2006)	Elastic catenary	−5.626	−0.860
Yang and Tsay (2007)	Elastic catenary	−5.625	−0.859
Thai and Kim (2011)	Elastic catenary	−5.626	−0.859
Abad et al. (2013)	Elastic catenary	−5.592	−0.855
Abad et al. (2013)	Elastic catenary	−5.626	−0.859
Present study	Elastic catenary	−5.626	−0.859
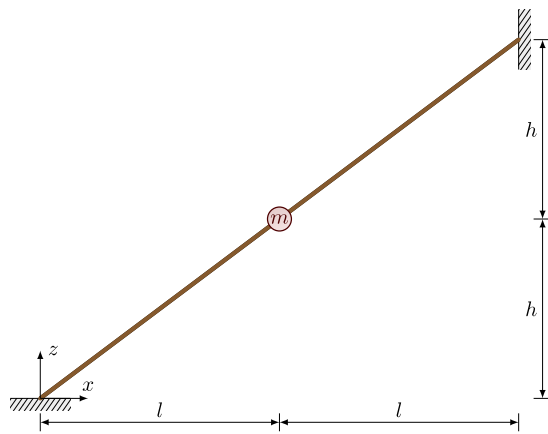
(a) Catenary cable elements.
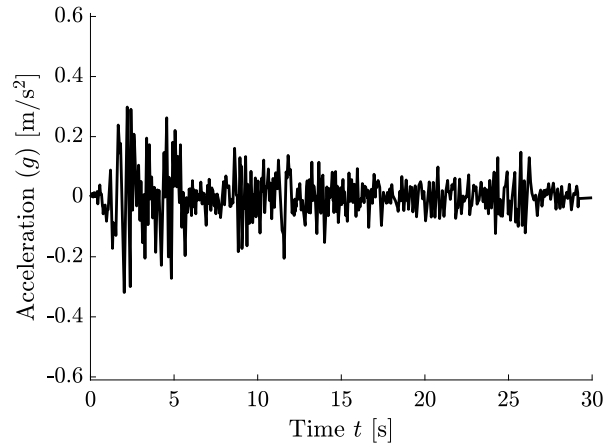
(b) Earthquake record of the EI Centro.

Fig. 11. Schematic model for an inclined cable system with the presence of an earthquake loading.
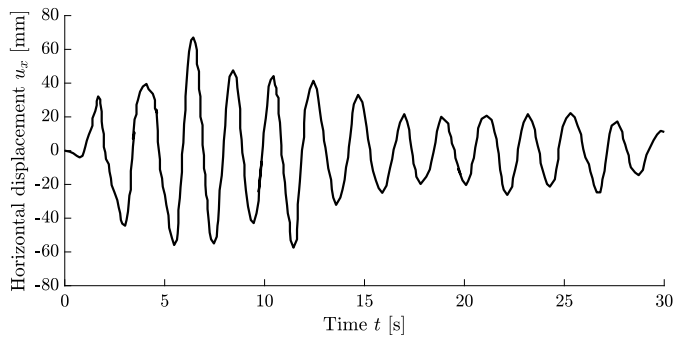
Fig. 12. Time evolution of the horizontal displacement u_x at the centre of inclined cable with the presence of an earthquake loading.

Table 3
Comparison of the peak displacement responses at the centre of inclined cable subjected to an earthquake loading.

Displacement (mm)		Thai and Kim (2011)		Present study
		Elastic catenary element	SAP2000	Elastic catenary element
Max	u_x	66.884	66.932	66.887
	u_z	77.076	77.038	77.078
Min	u_x	−57.730	−57.832	−57.733
	u_z	−89.093	−89.102	−89.095

gravitational acceleration $g = 9.81$ m/s^2, which are the same parameters as those adopted in Audusse et al. (2014). The mooring line has an

initial unstressed length $L_0 = 30$ m and we assume that the mooring line has a fixed anchor point and a fairlead point. Referring to previous study (Li and Choung, 2021a), the properties of the mooring line adopted in this study are summarized in Table 4.

Fig. 13(b) shows the spatial discretization of the computational domain of the shallow water-mooring line system using the proposed coupled method. Initially, the water domain is evenly discretized into 20 layers along the vertical direction whereas, a total number of 100 control volumes is adopted in the horizontal direction. The mooring line is equally divided into 30 segments with each having an unstrained length of 1 m. The total computational time of the simulation is 200 s. Fig. 14 illustrates the obtained water velocity fields and mooring line configurations at different instants using the proposed coupled method with water layers $N = 20$ and mooring line segments $M = 30$. In the presence of the considered wind-driven force on the water surface, the shallow water on the free-surface of the channel moves to the right direction. The flow gradually circulates when it flows and interacts with both closed right boundaries. As a result, the flow force leads to a dynamic motion of the mooring line along the flow direction. It can be observed that the top free-surface of the mooring line moves in the downwards direction. However, due to the recirculation of the water flow, the suspended mooring line at the bottom seabed of the channel is uplifted as the flow at the half-bottom of the channel recirculates from the right to the left. The good resolution of this fully coupled dynamic behaviour demonstrates the excellent performance of the proposed coupled model for the simulation of dynamics of the shallow water flow and the mooring line system.

To examine the influence of space discretization in the proposed coupled method, Tables 5 and 6 summarize the obtained maximum
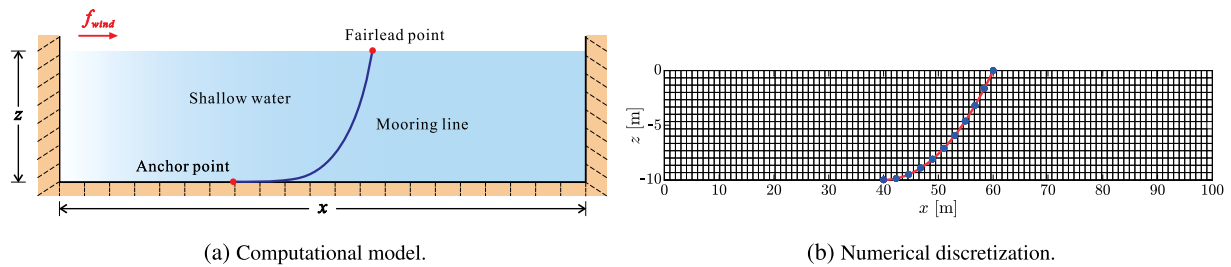
(a) Computational model.

(b) Numerical discretization.

Fig. 13. Computational model and numerical discretization for multilayer shallow water-mooring line system.

Table 4

Properties of the mooring line in the simulation of the wind-driven multilayer shallow water-cable system on a flat bottom.

Variable	Value	Variable	Value
Line diameter, D	0.0766 m	Tangential added mass coefficient, C_{at}	0.25
Line density, ρ	113.35 kg/m	Seabed stiffness coefficient per area, K_b	3.00×10^6 Pa/m
Line stiffness, EA	7.54×10^8 N	Seabed damping coefficient per area, C_b	5.20×10^6 Pa s/m
Normal drag coefficient, C_{dn}	2.00	Seabed friction coefficient, C_f	0.50
Tangential drag coefficient, C_{dt}	0.4	Seabed friction damping coefficient, D_f	200.00 N s/m
Normal added mass coefficient, C_{an}	0.8	Coefficient of mooring line, σ_m	0.0015

(a) $t = 0$ s

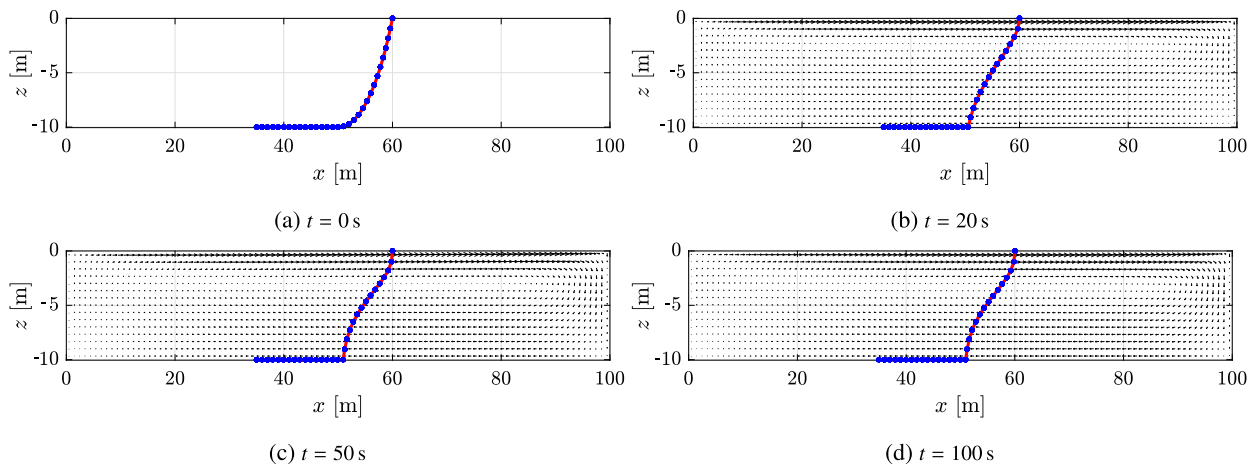(b) $t = 20$ s

(c) $t = 50$ s

(d) $t = 100$ s

Fig. 14. Water velocity fields and mooring line configurations obtained using the proposed fully coupled method with 20 water layers and 30 mooring line segments for the multilayer wind-driven shallow water-mooring system on a flat bottom.
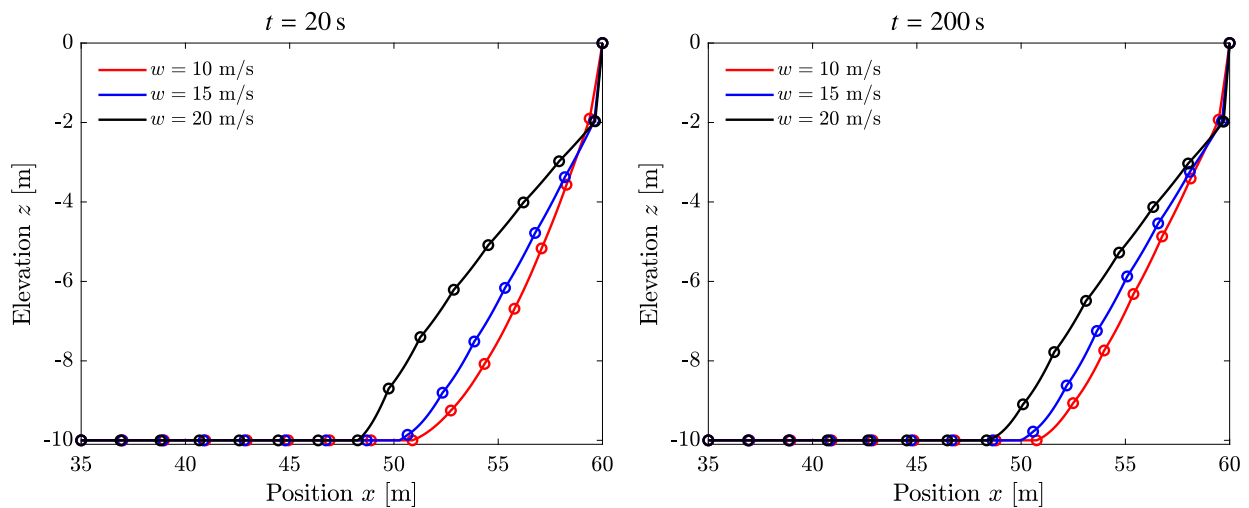

Fig. 15. Mooring line configurations under different wind speed w obtained by the proposed fully coupled model with $N = 30$ and $M = 15$ for the multilayer wind-driven shallow water-mooring system on a flat bottom.
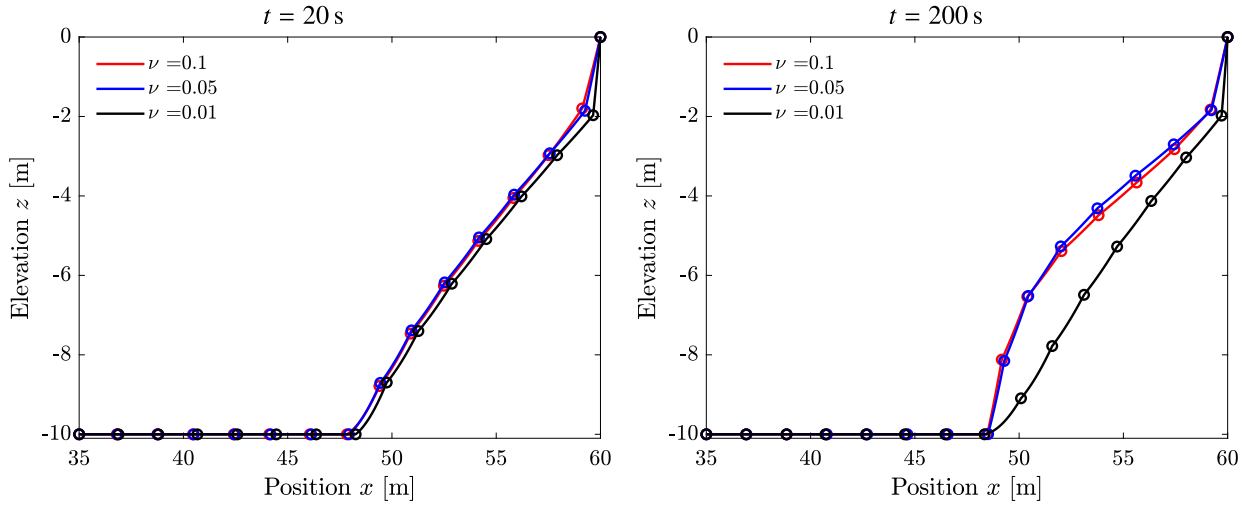
Fig. 16. Mooring line configurations with different values of water viscosity coefficients ν obtained by the proposed coupled model with $N = 30$ and $M = 15$ for the multilayer wind-driven shallow water-mooring system on a flat bottom.

Table 5
Computational results of multilayer wind-driven shallow water-mooring system on a flat bottom with water layers $N = 30$ and different values of the mooring segments M at four instants.

M	$t = 10\,\text{s}$		$t = 20\,\text{s}$		$t = 50\,\text{s}$		$t = 200\,\text{s}$	
	$\lvert\Delta u\rvert^m_{\max}$	$\lvert v\rvert^w_{\max}$	$\lvert\Delta u\rvert^m_{\max}$	$\lvert v\rvert^w_{\max}$	$\lvert\Delta u\rvert^m_{\max}$	$\lvert v\rvert^w_{\max}$	$\lvert\Delta u\rvert^m_{\max}$	$\lvert v\rvert^w_{\max}$
15	0.5683	3.0231	2.6021	4.7642	2.0583	5.4197	2.2329	5.4149
30	0.4768	3.0231	2.8317	4.7642	2.5127	5.4197	2.5775	5.4150
45	0.4776	3.0231	2.9514	4.7643	2.5755	5.4197	2.6457	5.4149

Table 6
Computational results of multilayer wind-driven shallow water-mooring system on a flat bottom with mooring line segments $M = 30$ and different values of the water layers N at four instants.

N	$t = 10\,\text{s}$		$t = 20\,\text{s}$		$t = 50\,\text{s}$		$t = 200\,\text{s}$	
	$\lvert\Delta u\rvert^m_{\max}$	$\lvert v\rvert^w_{\max}$	$\lvert\Delta u\rvert^m_{\max}$	$\lvert v\rvert^w_{\max}$	$\lvert\Delta u\rvert^m_{\max}$	$\lvert v\rvert^w_{\max}$	$\lvert\Delta u\rvert^m_{\max}$	$\lvert v\rvert^w_{\max}$
20	0.5100	2.3239	2.8409	3.9597	2.5742	4.8832	2.5742	4.8832
30	0.4768	3.0231	2.8317	4.7642	2.5127	5.4197	2.5775	5.4150
40	0.4796	3.4603	2.8893	5.1945	2.5767	5.7610	2.5767	5.7610

Fig. 17. Mooring line configurations at $t = 200\,\text{s}$ with different values of the friction coefficient σ_m using the proposed coupled method with $N = 30$ and $M = 30$ for the multilayer wind-driven shallow water-mooring system on a flat bottom.

values of nodal displacement of mooring line and shallow water velocity using different values of mooring segments M and water layers N, respectively. In both cases, the proposed coupled method captures the dynamic motion of the shallow water-mooring system with an obvious converging trend with an increased number of water layers and mooring segments. In Fig. 15, configurations of the mooring line at two different times $t = 20\,\text{s}$ and $t = 200\,\text{s}$ obtained by the proposed method using a wind speed of $V_{\text{wind}} = 10\,\text{m/s}$, $15\,\text{m/s}$, and $20\,\text{m/s}$ with $N = 30$ and $M = 15$. It can be seen that the values of V_{wind} have a significant influence on the dynamic motion of the mooring line system. As expected, a larger wind speed results in a larger flow force acting on the mooring line, which leads to larger displacements of the mooring system. In addition, the configuration difference gradually reduces as the computational time increases, which is due to the fact that accelerations of the water flow are gradually reduced and a steady-state flow is thus reached.

To demonstrate the influence of the water viscosity coefficient ν on the coupled system, Fig. 16 depicts the mooring line position obtained using the proposed method with three different values of ν varying from 0.01 to 0.1. It can easily be seen that the mooring line configurations are in great agreement with the different considered values of ν at $t = 20\,\text{s}$. However, a non-negligible difference in the mooring configurations is observed at the end of simulations. This is mainly related to the flow pattern associated with each value of the viscosity coefficient ν. It is expected that the velocity profile in the flow problem changes from straight to curved lines for small values of the viscosity coefficient. Weak exchange between the flow layers is also expected for small values of ν and this exchange becomes strong for large values of ν. Needless to mention that, solving the multilayer shallow water system without the mass exchange terms (*i.e.* $\mathcal{M} = 0$ and $\nu = 0$) yields a stationary flow which is identical to the one obtained using the conventional single-layer shallow water model.

To further explore the multilayer shallow water system with the presence of the mooring lines, Fig. 17 displays the final mooring line configurations with four different mooring friction coefficients, namely $\sigma_m = 0.5$, 0.15, 0.015, and 0.0015. It should be noted that with an increase in the values of σ_m, the frictional force term for shallow water accordingly increases, which further prevents the water flow and leads to a significantly reduced flow velocity. In contrast, as shown in Fig. 17, the change of σ_m shows small influences on the obtained final configuration of the mooring line system. Under the considered flow and mooring conditions, it has been shown that it is possible to resolve recirculation flow problems using only one global mass equation for the entire one-dimensional multilayer shallow water
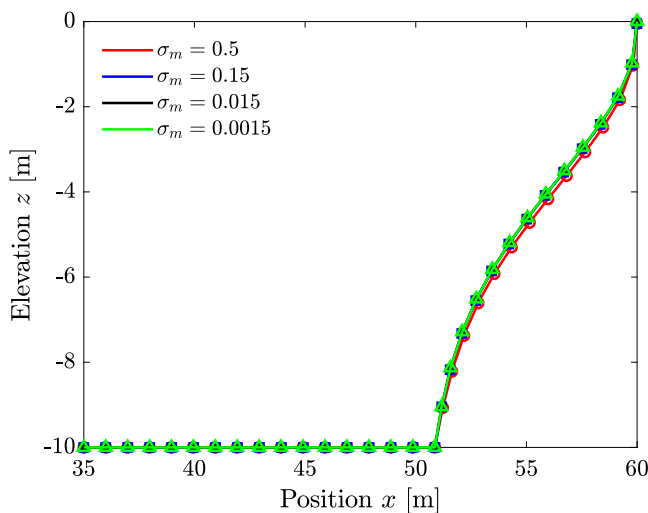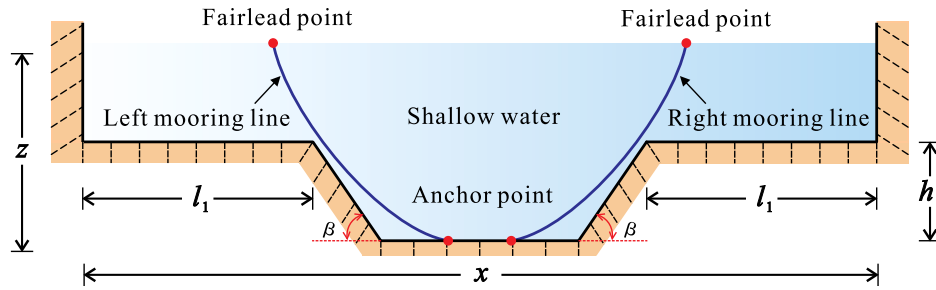
Fig. 18. Illustration of the multilayer wind-driven shallow water-mooring line system on a non-flat channel with two mooring lines.
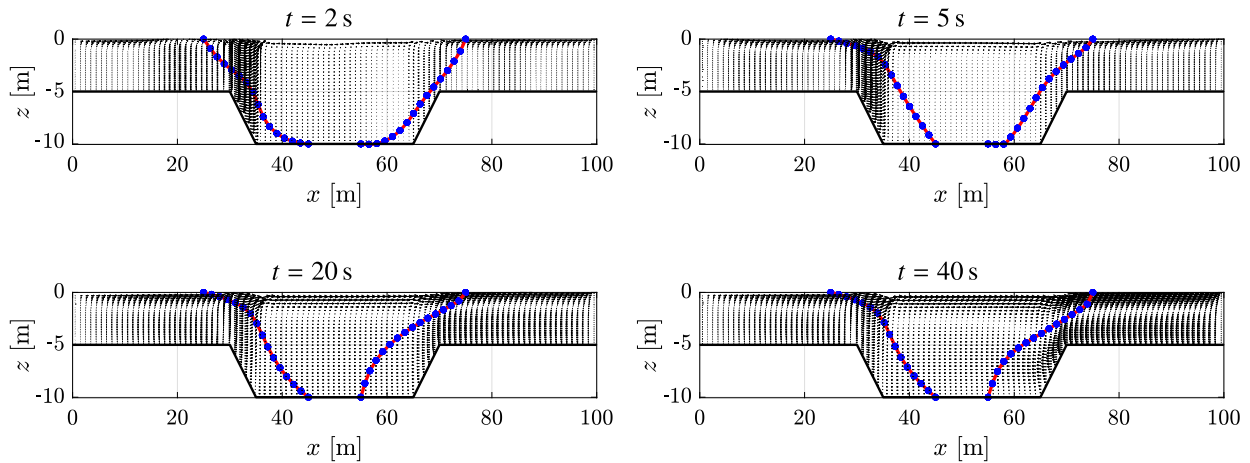

Fig. 19. Velocity fields and mooring line configurations for multilayer wind-driven shallow water-mooring system in a non-flat channel with two mooring lines.
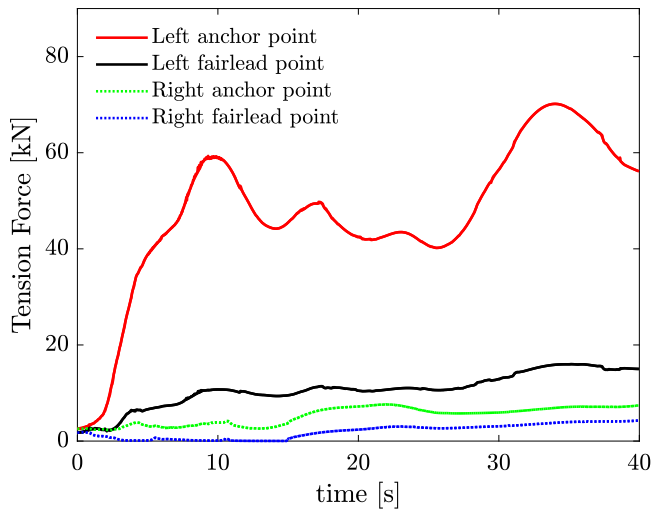

Fig. 20. Tension forces for multilayer wind-driven shallow water-mooring line system on a non-flat channel with two mooring lines.

system. The results obtained for this example also demonstrate that out coupled finite volume method and elastic catenary cable elements perform very satisfactorily for this shallow water-mooring line system since it does not produce excessive numerical dissipation in the flow fields and no spurious oscillations have been detected at the mooring lines in the computational domain.

4.6. Multilayer wind-driven shallow water-mooring system on a non-flat channel

In this example, analysis of multilayer wind-driven shallow water-cable system on a non-flat channel with two mooring lines is solved using the proposed coupled method. As shown in Fig. 18, the problem domain is defined by $x = 100$ m and $z = 10$ m. The non-flat bed of the channel is symmetric along the middle line of the problem domain and defined by $l_1 = 30$ m, $h_1 = 5$ m, and $\beta = 45°$. In our simulations, the density $\rho_w = 1000$ kg/m^3, the viscosity coefficient $\nu = 0.1$ m^2/s, the friction coefficient $\kappa = 1 \times 10^{-5}$ m/s, the wind stress coefficient $\sigma_s^2 = 1.5 \times 10^{-3}$, and the gravitational acceleration $g = 9.81$ m/s^2. Both mooring lines have an initial unstrained length of $L_0 = 23$ m, and their properties are given in Table 4.

Fig. 19 illustrates the obtained flow velocities and mooring line configurations at different times using the proposed coupled method with 20 water layers. Notice that both left and right mooring lines are evenly discretized into 15 segments with an initial unstrained length of 2.3 m for each segment. Similarly, with the presence of wind-driven force on the water surface, the water free-surface on the top part of the channel moves to the right direction. The flow gradually recirculates when it flows and interacts with both closed right boundaries and the non-flat bed. In addition, it can also be observed that the left mooring line is uplifted and becomes in tension after a short computational time. This is mainly due to a large jump of the flow velocity occurring at the local area above the left slope surface. This large jump can cause a large uplifting force that acts on the mooring line, and it can lead to a dynamic motion of the mooring line along the top-right direction. However, due to the recirculation of water flow, the right suspended mooring line at the bottom part of the channel is uplifted as the flow

at the half-bottom of the channel flows from the right to the left side, while the upper part moves in the right direction. Moreover, as shown Fig. 20, the tension forces at the anchor and fairlead points are also obtained from the proposed model, which can be directly used for the design of offshore platforms and mooring line systems. This computational results demonstrate the capability of the proposed method that can provide insight to coupled free-surface recirculation flows with mooring lines in large domains with non-flat beds. This simulation further demonstrates the high performance of the proposed coupled model for the simulation of the dynamic motion of the shallow water and mooring line system. Note that results from the proposed coupled model should be compared with observations of real dynamics within the water flow at the seabed. However, there is no such data available until now in the literature to carry out this work. Thus, at the moment we can only perform simulations and verify that results are plausible and consistent. In summary, the dynamics of mooring lines are captured accurately and the flow features are resolved reasonably. It should be stressed that all these excellent computational features are achieved using one-dimensional multilayer shallow water equations without requiring complex three-dimensional free-surface flow models.

5. Conclusions

In the present study, we have presented a novel numerical method for dynamic analysis of a fully coupled system of shallow water and mooring lines. The proposed method is based on an efficient and accurate coupled finite volume solver for multilayer shallow water flows to an elastic catenary cable element for the mooring line systems. Combining a class of robust velocity/acceleration projection and interpolation procedures, the proposed method addresses the key aspects for the modelling and simulation of interaction forces between the multilayer shallow water flow and the mooring line system. This would allow effects from the water flow to the mooring-line system and from the mooring-line system to the water flow through frictional transfer terms. Algorithmic details of the numerical formulation and implementation of the proposed coupled method have also been discussed in this study. Several numerical examples have been presented to examine the performance of these techniques. Computational results obtained for verification examples supported the conclusion that the proposed method can effectively be used to capture the dynamic motion of the shallow water and mooring line systems. In particular, two examples involving fully coupled shallow water-mooring line systems have been used to demonstrate the good performance of the developed coupled method. Further validations through comparison against experimental measurements (possibly obtained using centrifuge tests) and applications to coupled problems with more realistic seabed geometries will also be tackled in the future work. Extension of the proposed method to similar problems in three-dimensional domains using multilayer shallow water flows and catenary cable elements would also be subject of a future work.

CRediT authorship contribution statement

Xiangcou Zheng: Writing – original draft, Visualization, Validation, Software, Methodology, Formal analysis. **Mohammed Seaid:** Writing – review & editing, Supervision, Methodology, Funding acquisition, Conceptualization. **Ashraf S. Osman:** Writing – review & editing, Supervision, Methodology, Funding acquisition, Conceptualization.

Declaration of competing interest

The authors declare that they have no known competing financial interests or personal relationships that could have appeared to influence the work reported in this paper.

References

Abad, M.S.A., Shooshtari, A., Esmaeili, V., Riabi, A.N., 2013. Nonlinear analysis of cable structures under general loadings. Finite Elem. Anal. Des. 73, 11–19.

Abbott, M., 1979. Computational Hydraulics: Elements of the Theory of Free Surface Flows. Fearon-Pitman Publishers.

Amiri, S., Talebbeydokhti, N., Baghlani, A., 2013. A two-dimensional well-balanced numerical model for shallow water equations. Sci. Iran. 20 (1), 97–107.

Andreu, A., Gil, L., Roca, P., 2006. A new deformable catenary element for the analysis of cable net structures. Comput. Struct. 84 (29–30), 1882–1890.

API, R., 2001. 2SM, recommended practice for design, manufacture, installation, and maintenance of synthetic fiber ropes for offshore mooring.

Audusse, E., Benkhaldoun, F., Sari, S., Seaid, M., Tassi, P., 2014. A fast finite volume solver for multi-layered shallow water flows with mass exchange. J. Comput. Phys. 272, 23–45.

Audusse, E., Bristeau, M.-O., Pelanti, M., Sainte-Marie, J., 2011a. Approximation of the hydrostatic Navier-Stokes system for density stratified flows by a multilayer model: kinetic interpretation and numerical solution. J. Comput. Phys. 230 (9), 3453–3478.

Audusse, E., Bristeau, M.-O., Perthame, B., Sainte-Marie, J., 2011b. A multilayer Saint-Venant system with mass exchanges for shallow water flows. Derivation and numerical validation. ESAIM Math. Model. Numer. Anal. 45 (1), 169–200.

Benkhaldoun, F., Sari, S., Seaid, M., 2014. A simple multi-layer finite volume solver for density-driven shallow water flows. Math. Comput. Simulation 99, 170–189.

Benkhaldoun, F., Seaid, M., 2010. A simple finite volume method for the shallow water equations. J. Comput. Appl. Math. 234 (1), 58–72.

Bhinder, M.A., Karimirad, M., Weller, S., Debruyne, Y., Guérinel, M., Sheng, W., 2015. Modelling mooring line non-linearities (material and geometric effects) for a wave energy converter using AQWA, SIMA and Orcaflex. In: Proceedings of the 11th European Wave and Tidal Energy Conference, Nantes, France. pp. 6–11.

Bonaventura, L., Fernández-Nieto, E., Díaz, J., Narbona-Reinab, G., 2018. Multilayer shallow water models with locally variable number of layers and semi-implicit time discretization. J. Comput. Phys. 364, 209–234.

Codina, R., 1999. Numerical solution of the incompressible Navier–Stokes equations with coriolis forces based on the discretization of the total time derivative. J. Comput. Phys. 148, 467–496.

Gobat, J., Grosenbaugh, M., 2006. Time-domain numerical simulation of ocean cable structures. Ocean Eng. 33 (10), 1373–1400.

Gudmestad, O.T., Moe, G., 1996. Hydrodynamic coefficients for calculation of hydrodynamic loads on offshore truss structures. Mar. Struct. 9 (8), 745–758.

Harnois, V., Weller, S.D., Johanning, L., Thies, P.R., Le Boulluec, M., Le Roux, D., Soule, V., Ohana, J., 2015. Numerical model validation for mooring systems: Method and application for wave energy converters. Renew. Energy 75, 869–887.

Izem, N., Seaid, M., 2021. A well-balanced Runge-Kutta discontinuous Galerkin method for multilayer shallow water equations with non-flat bottom topography. Adv. Appl. Math. Mech. 14 (3), 725–758.

Jayaraman, H., Knudson, W., 1981. A curved element for the analysis of cable structures. Comput. Struct. 14 (3–4), 325–333.

Li, C.B., Choung, J., 2017. Fatigue damage analysis for a floating offshore wind turbine mooring line using the artificial neural network approach. Ships Offshore Struct. 12 (sup1), S288–S295.

Li, C.B., Choung, J., 2021a. Effects of strain-and strain rate-dependent nonlinear mooring line stiffness on floating platform motion. Ocean Eng. 241, 110011.

Li, C.B., Choung, J., 2021b. A new method of predicting hotspot stresses for longitudinal attachments with reduced element sensitivities. Int. J. Nav. Archit. Ocean Eng. 13, 379–395.

Li, C.B., Choung, J., Noh, M.-H., 2018. Wide-banded fatigue damage evaluation of Catenary mooring lines using various Artificial Neural Networks models. Mar. Struct. 60, 186–200.

Li, C.B., Seo, J.K., Paik, J.K., 2016. Proposed formulas for evaluation of the equivalent material properties of a multiholed structure. Ocean Eng. 121, 312–322.

Liu, W., Yunliang, B., Chao, W., Xin, L., 2018. Assessing the analytical solution of one-dimensional gravity wave model equations using dam-break experimental measurements. Water 10 (9).

Low, C.M., Ng, E.Y.-K., Narasimalu, S., Lin, F., Kim, Y., 2018. Numerical modelling of seabed impact effects on chain and small diameter mooring cables. Appl. Ocean Res. 80, 248–277.

Maffra, S.A.R.d.S., Pacheco, M.A.C., de Menezes, I.F.M., 2003. Genetic algorithm optimization for mooring systems. Generations 1, 3.

Michalos, J., Birnstiel, C., 1962. Movements of a cable due to changes in loading. Trans. Am. Soc. Civ. Eng. 127 (2), 267–282.

Newmark, N.M., 1959. A method of computation for structural dynamics. J. Eng. Mech. Div. 85 (3), 67–94.

O'Brien, W.T., Francis, A.J., 1965. Closure to "cable movements under two-dimensional loads". J. Struct. Div. 91 (4), 193–195.

Ozgen, I., Zhao, J., Liang, D., Hinkelmann, R., 2016. Urban flood modeling using shallow water equations with depth-dependent anisotropic porosity. J. Hydrol. 541, 1165–1184.

Sarpkaya, T., 1986. Force on a circular cylinder in viscous oscillatory flow at low Keulegan—Carpenter numbers. J. Fluid Mech. 165, 61–71.

Shankar, N., Cheong, H., Sankaranarayanan, S., 1997. Multilevel finite-difference model for three-dimensional hydrodynamic circulation. Ocean Eng. 24 (9), 785–816.

Soulard, T., Babarit, A., Borgarino, B., Wyns, M., Harismendy, M., 2013. C-HyP: A Combined wind and wave energy platform with balanced contributions. In: International Conference on Offshore Mechanics and Arctic Engineering. Vol. 55423, American Society of Mechanical Engineers, V008T09A049.

Sumer, B.M., et al., 2006. Hydrodynamics Around Cylindrical Strucures, vol. 26, World scientific.

Thai, H.-T., Kim, S.-E., 2011. Nonlinear static and dynamic analysis of cable structures. Finite Elem. Anal. Des. 47 (3), 237–246.

Tibert, G., 1998. Numerical Analyses of Cable Roof Structures. Dept. of Structural Engineering, Royal Institute of Technology.

Veritas, D.N., 2005. Guidelines on design and operation of wave energy converters. Carbon Trust.

Webster, W.C., 1995. Mooring-induced damping. Ocean Eng. 22 (6), 571–591.

Xiong, L., Li, X., Yang, J., Lu, W., 2018. Numerical simulation of nonlinearity and viscoelasticity of synthetic fibre rope for taut moorings in deep water. Ships Offshore Struct. 13 (2), 132–142.

Yan, J., Deng, X., Korobenko, A., Bazilevs, Y., 2017. Free-surface flow modeling and simulation of horizontal-axis tidal-stream turbines. J. Comput. Fluids 158, 157–166.

Yang, S.-H., Ringsberg, J.W., Johnson, E., 2014. Analysis of mooring lines for wave energy converters: A comparison of de-coupled and coupled simulation procedures. In: International Conference on Offshore Mechanics and Arctic Engineering. Vol. 45424, American Society of Mechanical Engineers, V04AT02A034.

Yang, Y., Tsay, J.-Y., 2007. Geometric nonlinear analysis of cable structures with a two-node cable element by generalized displacement control method. Int. J. Struct. Stab. Dyn. 7 (04), 571–588.

Zheng, X., Pisanò, F., Vardon, P.J., Hicks, M.A., 2021. An explicit stabilised material point method for coupled hydromechanical problems in two-phase porous media. Comput. Geotech. 135, 104112.

Zienkiewicz, O.C., Taylor, R.L., Zhu, J.Z., 2005. The Finite Element Method: Its Basis and Fundamentals. Elsevier, Oxford.

Zienkiewicz, O.C., Zhu, J., 1992a. The superconvergent patch recovery (SPR) and adaptive finite element refinement. Comput. Methods Appl. Mech. Engrg. 101 (1–3), 207–224.

Zienkiewicz, O.C., Zhu, J.Z., 1992b. The superconvergent patch recovery and a posteriori error estimates. Part 2: Error estimates and adaptivity. Internat. J. Numer. Methods Engrg. 33 (7), 1365–1382.